Implementation of a modified domain reduction technique as an engineering tool for site response analysis: method validation and verification under incident *SH* waves

Viviana Díaz Vélez
vdiazve@eafit.edu.co

Advisor:

Juan Gomez
Professor

Grupo de Mécanica Aplicada
Departamento de Ingeniería Civil
Universidad EAFIT
Medellín, Colombia
2015

CONTENTS

LIST OF FIGURES

LIST OF TABLES

Implementation of a modified domain reduction technique as an engineering tool for site response analysis: method validation and verification under incident *SH* waves

Viviana Diaz-Velez*

Disclaimer

This work corresponds to the research project conducted by the author within Grupo de Mecánica Aplicada at Universidad EAFIT and submitted in partial fulfillment of the requirements for the degree of Master of Science. The MsC program at Universidad EAFIT allows the authors to submit their works in a free format.

ABSTRACT

This work describes a computational framework to conduct site response analysis (SRA) including topographic effects and intended to be used by practicing engineers. The approach is based upon the domain reduction method (DRM) originally formulated by Bielak et al. (2003), in order to determine the response of small-scale localized topographic features present in large-scale seismic scenarios. Here we introduce additional assumptions into the reduction method, so it can be used with computational resources typically available at a consulting office. In particular, as suggested by the original DRM technique, we split the problem into a large-scale regional analysis and into a small-scale or local SRA. However, by contrast with the original approach, in our modified version of the method we include into the free-field the effect of the regional topography after generalizing the concept of the half-space. Subsequently, this free-field motion is used in the second step of the analysis and conducted to capture the effect of the small-scale (high frequency) topographic irregularities and the mechanical effect. For the local analysis we use

*Universidad EAFIT, Departamento de Ingeniería Civil. Medellín, Colombia

an homogenized version of the half-space, deviating once again from the original approach.

In this work we conduct a verification study of our modified DRM approach within the context of 2D topographies submitted to incident *SH* waves. For that purpose we have implemented the DRM algorithm into a commercial finite element analysis code having standard dynamic analysis capabilities. In order to test the applicability of the modified technique we selected idealized topographies amenable to be studied by geometrical methods.

INTRODUCTION

Local site effects, and particularly topographic effects, have been identified as one of the major causes of damage concentration in large urban areas during past and recent earthquakes. Classical examples of anomalous ground motion amplifications due to the presence of topographic variations at a site, can be identified in the large accelerations recorded at the Pacoima dam abutment during the 1971 San Fernando, California earthquake, (Trifunac & Hudson, 1971) and over the Tarzana Hill district, during the 1994 Northridge, California earthquake, (Bouchon & Barker, 1996). At the same time, the current number of deployed seismic instruments around the world has produced a large database of recorded evidence of the importance of topographic effects in the final ground response at a site (Gallipoli et al., 2014; Villalobos et al., 2011; Meslem et al., 2012; Hough et al., 2010; Laouami & Slimani, 2013; Maugeri et al., 2011; Assimaki et al., 2012).

Even though the problem of topographic site effects has been thoroughly studied by the scientific community during the last decades, the large amount of involved physical variables has resulted in important restrictions for its practical consideration at the engineering level when conducting site response analysis (SRA). Mathematically, the treatment of local effects upon the ground response at a site, implies the solution of a wave scattering problem formulated within a domain containing all possible complications such as complex shapes; heterogeneity of materials; variations in length scales; and complex constitutive responses. These inherent complexities seem to preclude the possibility of conducting SRA considering all the involved factors and particularly, those controlling the topographic effect, in terms of generalized guidelines that can be used for a wide variety of scenarios in seismic design regulations. For a review of existing methods for reliable ground estimation the reader is referred to Douglas & Aochi (2008).

A promising alternative, that has experienced a strong impetus during the last few years is the use of highly realistic numerical simulations. Such complex numerical models usually require a detailed description of the propagation path (i.e., given in terms of a large scale

geological velocity model), of the main earthquake sources potentially affecting the site and of the local soil deposits at which ground response analysis is desired, including details of surface and sub-surface topography. Such a complex set of input data is then used in combination with a high performance numerical solver in order to obtain ground motions for a specified region and under a variety of scenarios. Although realistic velocity models are already available for several sites around the world (Magistrale et al., 2000; Kohler et al., 2003; Wang et al., 2012; Jongmans et al., 1998; Paul et al., 2001; Ma et al., 2007; Fuis et al., 2001; Manakou et al., 2010; Raptakis et al., 2005; Dupros et al., 2010; Magistrale et al., 2008) and large scale solvers have seen a tremendous growth during the recent years (Ichimura et al., 2007; Lee et al., 2009b,a; Pilz et al., 2011; Bielak et al., 2010; Restrepo et al., 2012), the incorporation of these resources at the practicing level are still far from feasible. However, and regardless of the limitations of realistic models, there is an increasing need to develop and explore alternative solution methods that facilitate bridging the gap between these large scale efforts and the actual state of the practice making use of computational resources typically available at a consulting office. In other words, with the strong impetus of robust computational tools, there is also a growing need to transfer advanced simulation technology from the academic community to practicing engineers.

Among the recently developed numerical techniques to conduct numerical simulations over large scale realistic seismic scenarios, the multi-scale domain reduction method (DRM), formulated by Bielak et al. (2003) and tested and verified in Yoshimura et al. (2003b), seems highly appealing as an effective tool to incorporate the results from realistic simulations into the treatment of site effects by practicing engineers. The approach is a modular two-step algorithm which uses sub-structure ideas for the field and the spatial domain, in order to solve first a large scale model comprising the seismic source and the propagation path, but excluding from it the presence of localized features of soft material properties and small characteristic dimensions. The free field obtained during the large scale analysis step is then used as input excitation during subsequent analysis steps to be conducted over reduced (small scale) models including the local site. This DRM approach, has among others, the attractive feature that the large and reduced scale analyses can be performed in independent analysis steps and with different numerical techniques. Such independence creates the possibility of conducting the local SRA with computer resources typically available within a consulting office making the DRM approach very attractive as an actual engineering tool. Furthermore, the free field obtained from the large scale numerical model in the original formulation of the DRM may be replaced by consistent instrumental or field data in a way analogous to the existing one-dimensional techniques for SRA (Schnabel et al., 1972). Moreover, in an ongoing effort the authors are developing techniques where free-field ground motions consistent with specified uniform seismic hazard response spectra are obtained in order to produce results equivalent to those from the large scale analysis.

Implementations of the DRM technique by other authors and its application to a variety of problems can be identified in the works of Jeremic (2004), Preisig & Jeremić (2005), Elgamal et al. (2008), Jeremić et al. (2009), Jeremic (2010). For instance Jeremic (2004) implemented and applied the DRM method into the computational framework OPENSEES in order to study soil-foundation-structure interaction (SFSI) problems using a large scale geophysical wave propagation model to study the earthquake response of bridges. On the other hand, Preisig & Jeremić (2005) applied this formulation to conduct non-linear SFSI analysis into the DRM formalism. Elgamal et al. (2008) created a similar model to evaluate the seismic response of the Humboldt Bay Bridge using also the OPENSEES platform. These authors excited the model using a traditional approach but suggested that the response evaluation could be improved provided the seismic excitation was applied following the DRM technique. Jeremić et al. (2009) also used the DRM algorithm in the analysis of a long-span bridge with an input motion corresponding to a vertically incident wave field. They assumed surface free-field ground motions and used a deconvolution approach to transfer these motions to a depth $100m$ below the surface. Then, a vertically propagating wave field was created and used to compute effective DRM forces to apply into the bridge model. Finally Jeremic (2010) discussed energy dissipation in structures by different mechanisms and used as high fidelity simulation tool to test these mechanisms a DRM approach.

The accuracy of the original DRM algorithm hinges on the material exterior to the region Ω, corresponding to the localized feature in the reduced domain, being identical to that in the original problem. In our modified version the local site preserves all the small scale topographic irregularities, but in contrast to the original approach, the localized feature is assumed supported by a perfect homogeneous half-space, whereby all the interaction between the large scale and local topography is removed. For instance, although in the original DRM formulation the background or auxiliary problem used to obtain the free field response is an arbitrary structure, all the verification problems presented in Yoshimura et al. (2003a) correspond to isolated localized topographic features. The consideration of these two deviations from the original technique lead to our modified version of the DRM. As such, we asses the capabilities of this simpler version of the DRM as a possible analysis tool for the effective consideration of site effects at the practicing level. For that purpose we assume that the numerical results from a large-scale simulation are available and stored as a database of effective excitations, associated to a realistic seismic region (e.g., a urban area and its related seismic sources) and ready to be used in a simplified local analysis step with the aid of commercial numerical packages.

In this work we conduct the local analysis using the finite element code FEAP. First, and in order to validate the correctness of the implementation we found the response of a 30^0 V-shaped canyon submitted to incident *P*, *SV* and *SH* plane waves. Although all of these problems could be solved in a single analysis step, where the incoming motion is obtained in closed

form, we used these solutions as a transparency test. Second, we conducted our verification study, intended to identify the range of applicability of the modified DRM algorithm. For that purpose we conducted a series of analysis under plane wave incidence over strongly idealized topographies submitted to *SH* waves. An idealized topography combined with a simple *SH* wave field is substantiated on the fact that such class of problems can be studied by simple ray theory methods. In this study we separated the total solution into optical and diffracted contributions as proposed in Gomez et al. (2013). That separation is convenient as it helps us identify parts of the domain where the solution is expected to be difficult to reproduce by an approximated method. In this sense we selected as a regional (or large scale) topography a 60^0 V-shaped canyon since for this particular slope the canyon produces an over-illuminated zone in the supporting half-space. Subsequently and resembling the localized topographic feature, we placed a small semi-circular canyon at different positions relative to the regional canyon containing the over-illuminated zone.

This report is organized as follows. In the first section we review the relevant aspects of the original DRM method, starting with the classical formulation of the wave scattering problem. We describe also the verification problems considered by Yoshimura et al. (2003a) in order to highlight the aspects where our approach deviates from the original one. Then we formulate and implement our modified version of the DRM algorithm. The verification study, including a ray theory solution is then presented for the 60^0 V-shaped canyon. The report concludes with a discussion and recommendations for further work.

DOMAIN REDUCTION METHOD

Classical formulation of the scattering problem

In order to have a general context of the physical basis of the DRM technique formulated by Bielak et al. (2003) it is convenient to describe the so-called scattering problem in elastodynamics. We will use an integral equation approach based on the elastodynamics representation theorem (Pao & Varatharajulu, 1976). The physical problem is schematized by the top part of fig. 1 which depicts a generalized half-space with domain Ω^+ supporting a scatterer with domain Ω. Both domains are bounded through the perfectly coupled surface Γ and the remote boundary of the half-space Γ^+. Notice that the scatterer also comprises a localized, small-scale topographic feature (e.g., a microzone) embedded into a large topographic irregularity. The scattering problem consists in determining the response of the system when it is submitted to the action of an incident wave.

The domain reduction method, originally formulated by Bielak et al. (2003) and verified in Yoshimura et al. (2003b) is a two-step algorithm developed for the simulation of earthquake

ground motions in seismic scenarios containing strong variations in wavelength. The fundamental principle underlying the method is the classical partition of the field used in the formulation of scattering problems (Pao & Varatharajulu, 1976; Courant & Hilbert, 2008; Bielak & Christiano, 1984) written like ;

$$u = u^0 + w \tag{1}$$

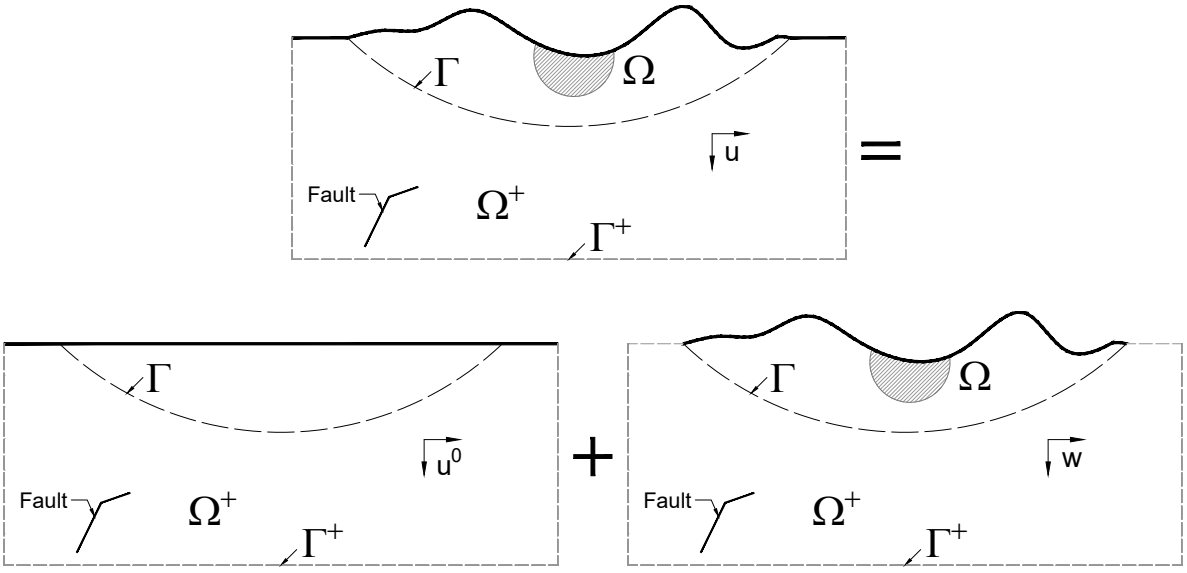

Figure 1: Partition of the field in the classical definition of the scattering problem. The free-field u^0 corresponds to the response of the half-space with the scatterer being removed (bottom left), while the scattered field w would be the additional displacement introduced in the half-space once the scatterer Ω is considered (bottom right).

where u^0 is the free field motion or response of the half-space in the absence of the scatterer and w is a scattered field or relative displacement motion between the total and free-field motion. This free field motion can be obtained in closed-form depending on the nature of the half-space and of the seismic excitation. In the more general case it is also found numerically from the solution of the simpler problem described in the bottom left of fig. 1.

Following the elastodynamics representation theorem the boundary value problem for the total field inside the scatterer is governed by;

$$C_{ij}(\vec{\xi})u_j(\vec{\xi}) = \int_{\Gamma} G_{ij}^{FS}(\vec{x};\vec{\xi})t_j(\vec{x})dS(\vec{x}) - \int_{\Gamma^+ + \Gamma} H_{ij}^{FS}(\vec{x};\vec{\xi})u_j(\vec{x})dS(\vec{x}) \quad \text{for } \vec{\xi} \text{ inside } \Gamma^+ \cup \Gamma \tag{2}$$

and where G_{ij}^{FS} and H_{ij}^{FS} are the full-space displacements and tractions Green's tensors respectively while C_{ij} is a tensor which depends on the smoothness of the boundary and u_i

and t_i are the total displacements and tractions vectors. Similarly, the relative motion in the half-space w_i is governed by;

$$C_{ij}(\vec{\xi})w_j(\vec{\xi}) = \int_\Gamma G_{ij}^{HS}(\vec{x};\vec{\xi})t_j^w(\vec{x})dS(\vec{x}) - \int_\Gamma H_{ij}^{HS}(\vec{x};\vec{\xi})w_j(\vec{x})dS(\vec{x}) \quad \text{for } \vec{\xi} \text{ inside } S_F \cup \Gamma^+ \cup \Gamma \tag{3}$$

where now G_{ij}^{HS} and H_{ij}^{HS} are the corresponding Green's tensors for the half-space. Notice that the excitation enters into the problem once the surface compatibility conditions;

$$\begin{aligned} u &= u^0 + w \\ t &+ t^0 + t_w = 0 \end{aligned} \tag{4}$$

are imposed along Γ.

Bielak et al(2003) DRM algorithm

For completeness we describe in this section the original DRM formulation as proposed by Bielak et al. (2003). The problem is schematized by the top part of fig. 2 which depicts a generalized half-space with domain Ω^+ supporting a scatterer Ω. Both domains are bounded through the perfectly coupled surface Γ. Notice that the scatterer comprises also a localized, small-scale topographic feature (e.g., a microzone) embedded into a large topographic irregularity. The relevant degrees of freedom have been labeled after Bielak et al. (2003). In this work we are interested in conducting SRA at the microzone.

The partitioned equations of motion for the half-space and scatterer (i.e., Ω) read;

$$\begin{bmatrix} M_{ii}^{\Omega} & M_{ib}^{\Omega} \\ M_{bi}^{\Omega} & M_{bb}^{\Omega} \end{bmatrix} \begin{Bmatrix} \ddot{u}_i \\ \ddot{u}_b \end{Bmatrix} + \begin{bmatrix} K_{ii}^{\Omega} & K_{ib}^{\Omega} \\ K_{bi}^{\Omega} & K_{bb}^{\Omega} \end{bmatrix} \begin{Bmatrix} u_i \\ u_b \end{Bmatrix} = \begin{Bmatrix} 0 \\ P_b \end{Bmatrix} \tag{5}$$

$$\begin{bmatrix} M_{bb}^{\Omega^+} & M_{be}^{\Omega^+} \\ M_{eb}^{\Omega^+} & M_{ee}^{\Omega^+} \end{bmatrix} \begin{Bmatrix} \ddot{u}_b \\ \ddot{u}_e \end{Bmatrix} + \begin{bmatrix} K_{bb}^{\Omega^+} & K_{be}^{\Omega^+} \\ K_{eb}^{\Omega^+} & K_{ee}^{\Omega^+} \end{bmatrix} \begin{Bmatrix} u_b \\ u_e \end{Bmatrix} = \begin{Bmatrix} -P_b \\ P_e \end{Bmatrix} \tag{6}$$

where P_b are nodal forces through the coupling surface Γ, P_e represent the loads induced by a seismic source or by an incident plane wave and M and K are finite element mass and stiffness matrices. Coupling eq. (5) and eq. (6) yields the complete system of equations governing the half-space-scatterer system subjected to an exterior seismic source P_e and solved in one step algorithms (i.e., without DRM);

$$\begin{bmatrix} M_{ii}^{\Omega} & M_{ib}^{\Omega} & 0 \\ M_{bi}^{\Omega} & M_{bb}^{\Omega}+M_{bb}^{\Omega^+} & M_{be}^{\Omega^+} \\ 0 & M_{eb}^{\Omega^+} & M_{ee}^{\Omega^+} \end{bmatrix} \begin{Bmatrix} \ddot{u}_i \\ \ddot{u}_b \\ \ddot{u}_e \end{Bmatrix} + \begin{bmatrix} K_{ii}^{\Omega} & K_{ib}^{\Omega} & 0 \\ K_{bi}^{\Omega} & K_{bb}^{\Omega}+K_{bb}^{\Omega^+} & K_{be}^{\Omega^+} \\ 0 & K_{eb}^{\Omega^+} & K_{ee}^{\Omega^+} \end{bmatrix} \begin{Bmatrix} u_i \\ u_b \\ u_e \end{Bmatrix} = \begin{Bmatrix} 0 \\ 0 \\ P_e \end{Bmatrix} \tag{7}$$

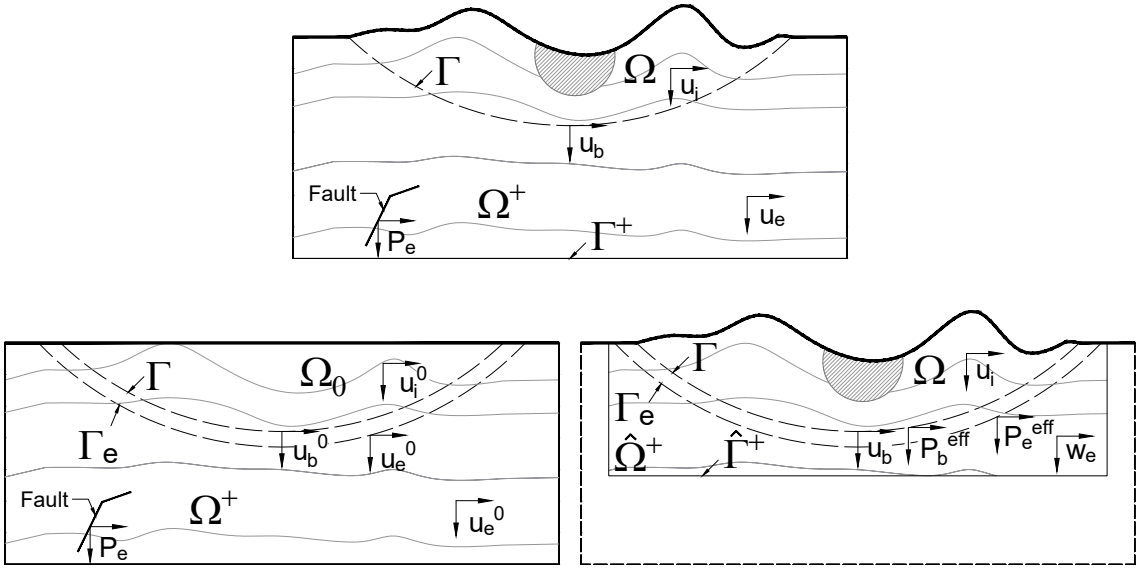

Figure 2: Generalized partition of the total domain and its related fields in the original DRM algorithm. The first analysis step is conducted over the half-space with domain $\Omega^+ \cup \Omega_0$ (bottom left). The resulting motion is then applied as input excitation to the reduced domain $\hat{\Omega}^+ \cup \Omega$ comprising only the localized feature (bottom right).

In the original DRM method the effect of the seismic sources P_e is transferred to the coupling surface Γ using an auxiliary problem (or background structure) constructed after removing from the complete domain the scatterer Ω and replacing it by an arbitrary simplified domain Ω_0 resulting in a generalized half-space $\Omega^+ \cup \Omega_0$ (as shown in the left part of fig. 2). This arbitrary domain is selected in such a way that it is easier to discretize than the original problem. The equations of motion for the domain Ω^+ in the auxiliary problem under the action of the seismic sources P_e yields a generalized free field motion u^0 governed by;

$$\begin{bmatrix} M_{bb}^{\Omega^+} & M_{be}^{\Omega^+} \\ M_{eb}^{\Omega^+} & M_{ee}^{\Omega^+} \end{bmatrix} \begin{Bmatrix} \ddot{u}_b^0 \\ \ddot{u}_e^0 \end{Bmatrix} + \begin{bmatrix} K_{bb}^{\Omega^+} & K_{be}^{\Omega^+} \\ K_{eb}^{\Omega^+} & K_{ee}^{\Omega^+} \end{bmatrix} \begin{Bmatrix} u_b^0 \\ u_e^0 \end{Bmatrix} = \begin{Bmatrix} -P_b^0 \\ P_e \end{Bmatrix} \tag{8}$$

allowing to express the seismic sources like;

$$P_e = M_{eb}^{\Omega^+} \ddot{u}_b^0 + M_{ee}^{\Omega^+} \ddot{u}_e^0 + K_{eb}^{\Omega^+} u_b^0 + K_{ee}^{\Omega^+} u_e^0. \tag{9}$$

The presence of the terms $M_{ee}^{\Omega^+} \ddot{u}_e^0$ and $K_{ee}^{\Omega^+} u_e^0$ in eq. (9) imply that the free field u^0 must be stored throughout the full domain Ω^+. This inconvenient requirement is dealt with after

writing the total field in the exterior part of Ω^+ like a superposition of the free field motion u_e^0 and the relative (or scattered) motion w_e as;

$$u_e = u_e^0 + w_e \tag{10}$$

which yields;

$$\begin{bmatrix} M_{ii}^{\Omega} & M_{ib}^{\Omega} & 0 \\ M_{bi}^{\Omega} & M_{bb}^{\Omega}+M_{bb}^{\Omega^+} & M_{be}^{\Omega^+} \\ 0 & M_{eb}^{\Omega^+} & M_{ee}^{\Omega^+} \end{bmatrix} \begin{Bmatrix} \ddot{u}_i \\ \ddot{u}_b \\ \ddot{w}_e \end{Bmatrix} + \begin{bmatrix} K_{ii}^{\Omega} & K_{ib}^{\Omega} & 0 \\ K_{bi}^{\Omega} & K_{bb}^{\Omega}+K_{bb}^{\Omega^+} & K_{be}^{\Omega^+} \\ 0 & K_{eb}^{\Omega^+} & K_{ee}^{\Omega^+} \end{bmatrix} \begin{Bmatrix} u_i \\ u_b \\ w_e \end{Bmatrix} = \begin{Bmatrix} 0 \\ -M_{be}^{\Omega^+}\ddot{u}_e^0 - K_{be}^{\Omega^+}u_e^0 \\ P_e - M_{ee}^{\Omega^+}\ddot{u}_e^0 - K_{ee}^{\Omega^+}u_e^0 \end{Bmatrix} \tag{11}$$

After substituting for P_e from eq. (9) into eq. (11) the equations of motion are written in terms of degrees of freedom over a single layer of finite elements in Ω^+ adjacent to Γ. This strip of 1-element width lies between Γ and its adjacent surface Γ_e (see fig. 2);

$$\begin{bmatrix} M_{ii}^{\Omega} & M_{ib}^{\Omega} & 0 \\ M_{bi}^{\Omega} & M_{bb}^{\Omega}+M_{bb}^{\Omega^+} & M_{be}^{\Omega^+} \\ 0 & M_{eb}^{\Omega^+} & M_{ee}^{\Omega^+} \end{bmatrix} \begin{Bmatrix} \ddot{u}_i \\ \ddot{u}_b \\ \ddot{w}_e \end{Bmatrix} + \begin{bmatrix} K_{ii}^{\Omega} & K_{ib}^{\Omega} & 0 \\ K_{bi}^{\Omega} & K_{bb}^{\Omega}+K_{bb}^{\Omega^+} & K_{be}^{\Omega^+} \\ 0 & K_{eb}^{\Omega^+} & K_{ee}^{\Omega^+} \end{bmatrix} \begin{Bmatrix} u_i \\ u_b \\ w_e \end{Bmatrix} = \begin{Bmatrix} 0 \\ -M_{be}^{\Omega^+}\ddot{u}_e^0 - K_{be}^{\Omega^+}u_e^0 \\ M_{eb}^{\Omega^+}\ddot{u}_b^0 + K_{eb}^{\Omega^+}u_b^0 \end{Bmatrix} \tag{12}$$

The actual domain reduction leading to the method in the formulation from Bielak et al. (2003) is possible after noticing that all the waves in the exterior region Ω^+ are outgoing. Since the primary interest is in the determination of the response for the local site (i.e., a microzone) this fact suggests that the size of Ω^+ can be drastically reduced. This exterior reduced domain in the DRM algorithm is termed $\hat{\Omega}^+$.

The following points regarding the DRM formulation must be highlighted. First the equations of motion given in eq. (7) when written in terms of the free field motion reads:

$$\begin{bmatrix} M_{ii}^{\Omega} & M_{ib}^{\Omega} & 0 \\ M_{bi}^{\Omega} & M_{bb}^{\Omega}+M_{bb}^{\Omega^+} & M_{be}^{\Omega^+} \\ 0 & M_{eb}^{\Omega^+} & M_{ee}^{\Omega^+} \end{bmatrix} \begin{Bmatrix} \ddot{u}_i \\ \ddot{u}_b \\ \ddot{u}_e \end{Bmatrix} + \begin{bmatrix} K_{ii}^{\Omega} & K_{ib}^{\Omega} & 0 \\ K_{bi}^{\Omega} & K_{bb}^{\Omega}+K_{bb}^{\Omega^+} & K_{be}^{\Omega^+} \\ 0 & K_{eb}^{\Omega^+} & K_{ee}^{\Omega^+} \end{bmatrix} \begin{Bmatrix} u_i \\ u_b \\ u_e \end{Bmatrix} = \begin{Bmatrix} 0 \\ 0 \\ M_{eb}^{\Omega^+}\ddot{u}_b^0 + M_{ee}^{\Omega^+}\ddot{u}_e^0 + K_{eb}^{\Omega^+}u_b^0 + K_{ee}^{\Omega^+}u_e^0 \end{Bmatrix}. \tag{13}$$

However complete transfer of the seismic sources P_e to the coupling surface Γ is only achieved after one eliminates from eq. (13) the terms $M_{ee}^{\Omega^+}\ddot{u}_e^0$ and $K_{ee}^{\Omega^+}u_e^0$ which is accomplished by introducing the change of variables resulting after writing the total field in the exterior part of Ω^+ in terms of the free-field and relative motion. For this change of variables to remain valid it is required that the reduced exterior domain $\hat{\Omega}^+$ retains the same material properties as the original exterior domain Ω^+. The resulting DRM approach can be summarized in the following two-step algorithm:

- In step-I the complete seismic domain $\Omega \cup \Omega^+$, comprising the seismic source and microzones of soft material properties is replaced by a simpler domain $\Omega_0 \cup \Omega^+$ which results after removing all the surface topography and localized features.

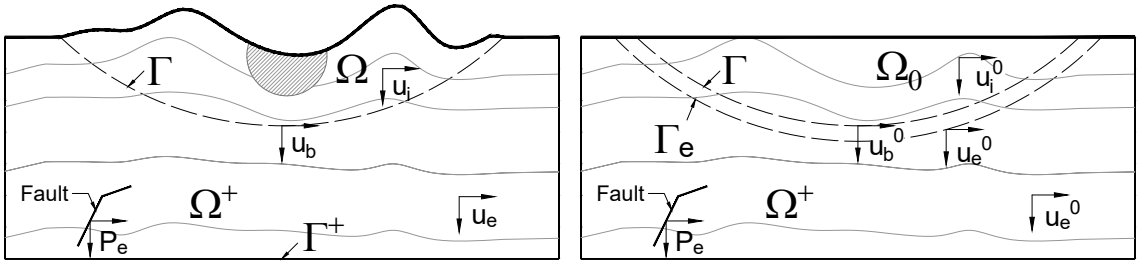

Figure 3: In step I of the DRM algorithm the original domain $\Omega \cup \Omega^+$ (left) is replaced by a simpler domain $\Omega_0 \cup \Omega^+$ (right).

This simpler domain is analyzed, under the action of seismic sources P_e, in order to determine the free field response leading to effective loads located over a boundary adjacent to the local site given by;

$$P^{eff} = \left\{ \begin{array}{c} 0 \\ -M_{be}^{\Omega^+}\ddot{u}_e^0 - K_{be}^{\Omega^+}u_e^0 \\ M_{eb}^{\Omega^+}\ddot{u}_e^0 + K_{ee}^{\Omega^+}u_e^0 \end{array} \right\}. \tag{14}$$

Although in the original DRM formulation this new domain is arbitrary, in the verification problems presented in Yoshimura et al. (2003b) only domains with a single topographic irregularity were analyzed. As a result the simpler domain assumed in all the cases the form of a half-space with all the surface topography being removed.

- In step-II of the algorithm, ground response analysis is performed at desired microzones using as excitation the free-field motion extracted from the data base created during step-I.

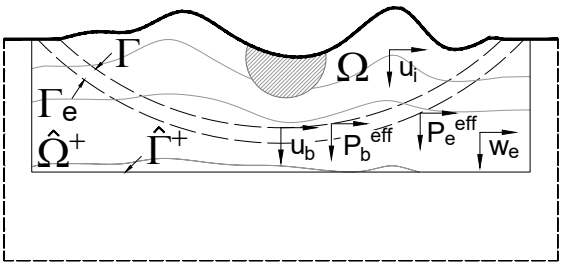

Figure 4: Reduced domain subjected to the action of effective forces P^{eff} and equivalent to the seismic sources.

The local model can take into account a highly detailed description of the small-scale topography. This local step can be performed using computing resources typically available at a consulting office and using an independent numerical technique.

A key aspect in the DRM technique is the fact that in the reduced domain $\hat{\Omega}^+ \cup \Omega$, the domain $\hat{\Omega}^+$ is of the same material properties as in the original Ω^+ (right part of fig. 2). To reflect this fact the mass and stiffness coefficients pertaining to the domain $\hat{\Omega}^+$ have retained the superscript Ω^+.

Verification cases considered by Yoshimura et al. (2003a)

In order to identify the differences between our modified approach (to be presented later) and the original DRM technique, it is important to describe briefly the verification study conducted by Yoshimura et al. (2003a). These authors tested the accuracy behind the DRM technique in several three-dimensional (3D) problems. First, they conducted a transparency test using a flat layered system. The authors solved the problem using the DRM algorithm and a boundary element method (BEM) formulation. Applicability of the DRM technique was later demonstrated by replacing Ω in step-II with different local structures. The analysis was conducted for a maximum frequency of $1.0Hz$. The results revealed maximum differences in amplitude on the order of 5% between the two approaches. Since for this problem there is no physical scattering field, such condition was used as a verification test and it was shown to be satisfied by the finite element solution which effectively showed the outgoing waves to vanish outside of the internal surface Γ.

As a second verification example the authors solved the problem of a basin with the shape of a spherical cap embedded in the layered system used for the transparency test. Since the same seismic source was considered in both analysis, recalculation of the free field motion was unnecessary. In order to prevent the scattered waves generated by the basin from reflecting back into the interior domain, absorbing boundaries were used along the surface $\hat{\Gamma}^+$. A primary indication of the correctness of the method was the fact that the wave motion outside the basin

was purely outgoing. In order to test the applicability of the method to deal with topographic irregularities, the authors also determined the response of a squared-based hill resting on top of the stratified half-space. In a first numerical test they used a hill with the same material properties as the top layer of the stratified system, while in the second example they added to the hill a $25.0m$ thick weathered surface. The main observation resulting from these examples, and identified as an attractive feature of the DRM method, is the relative efficiency of the associated absorbing boundary conditions since in the DRM technique the problem is specified with unknowns outside of the region of interest corresponding to the residual field only. As reported by the authors, it appears that such perturbation can be small even if the properties of the localized feature differ significantly from those of the background structure. In these cases the absorbing boundaries are required to dissipate only a small amount of energy with respect to the free field motion.

As a final example the verification study addressed a more realistic seismic scenario comprised by $80-km$ x $80-km$ x $30-km$ region enclosing the Los Angeles basin. In this case the free field motion, or response of the background structure was also determined numerically due to the highly heterogeneous material properties for the basin. The velocity model corresponded to the southern California reference 3D seismic velocity model, version 2 (Magistrale et al., 2000), developed at the Southern California Earthquake Center. No surface topography was included and in order to test the DRM methodologies they considered a region of interest (microzone) of dimensions $6-km$ x $6-km$ x $0.5-km$. The verification analysis followed the two steps of the DRM method including large scale simulation to determine the free-field in a background structure; and small-scale determination of the response of the localized feature. Time domain results from the DRM and the traditional approach were compared for various receivers along the computational domain. In this particular problem the authors implemented an interpolation scheme in order to deal with the space incompatibilities between the large and the small scale meshes. As pointed out in that study, even though the material properties within the localized region were almost uniform in the lateral direction, the spatial variability of the surface ground motion was quite strong. This strong variation was perfectly captured by the DRM approach.

Two important points must be mentioned regarding the verification study. First, as expressed by Yoshimura et al. (2003a) the DRM technique is capable of dealing with problems in which some portions of the domain have very low shear-wave velocity compared to that of the background structure, allowing the user to implement coarser meshes for the auxiliary system than would be needed in a single step procedure. Second, the fact that the verification study did not addressed any problems in which there were several topographic irregularities, of various length scales intercalating between each other. In our proposed modified DRM approach, the background structure retains some large scale topographic features whose effect is expected

to be captured by the free field. In step-II of the modified technique, the effect of the large scale topography is then applied in the form of effective forces into the local SRA. Finally, in the verification study the condition of having a background structure Ω^+ and a reduced exterior domain $\hat{\Omega}^+$ with the same material properties was always satisfied, while in our proposed modified approach the reduced domain is replaced by an homogenized version of $\hat{\Omega}^+$.

Modified DRM algorithm

It must be pointed out that the main purpose behind the idea of formulating a simplified DRM approach, is to obtain an analysis technique for SRA that can be used by practicing engineers without access to large computational resources, but limited to the standard computational capabilities of a consulting office. In this sense, it is assumed that the free field motion u^0 required during step-I of the original DRM technique is available from an external source. For instance, this free field may have been obtained out of a database of results generated after a large scale simulation of a seismic region performed by an independent source or may be the result of instrumental data filtered through a simpler homogenized version of the large scale scenario. In any case, the free field motion is not the result of a computation performed by the practicing engineer during the actual process of conducting SRA at the micro-zone. However, in order to clearly indicate the differences between the original and modified approaches the full problem is described again.

In the modified DRM algorithm the concept behind the free-field motion is applied in a more general sense. Here the supporting half-space is considered like a generalized half-space comprising not only the earthquake source but also relatively large topographic features of characteristic length L. This would produce a free-field motion carrying with it information about large topographic effects. We refer to this free-field motion as the regional field u^R. Similarly, denoting the characteristic dimensions of the topographic irregularities at the local site by ℓ, implicitly introduces an arbitrary division of half-space and microzone in terms of soft and hard material properties and of characteristic dimensions L and ℓ. For instance, the generalized half-space could be defined like the part of the total domain that is left after one removes all the sub-domains with shear wave propagation velocity $\beta \leq \beta^0$ and with $\ell \leq \ell^0$ where β^0 and ℓ^0 are predefined values for the shear wave velocity and characteristic dimension respectively. In the extreme case in which $\ell^0 \to \infty$ and β^0 is the largest S-wave propagation velocity present in the problem, the generalized half-space will collapse into the classical idealized half-space. This process is schematized in fig. 5 where we show once again the full problem (top), the modified auxiliary domain, containing now large topographic irregularities (bottom left) and the reduced domain containing only the microzone (bottom right).

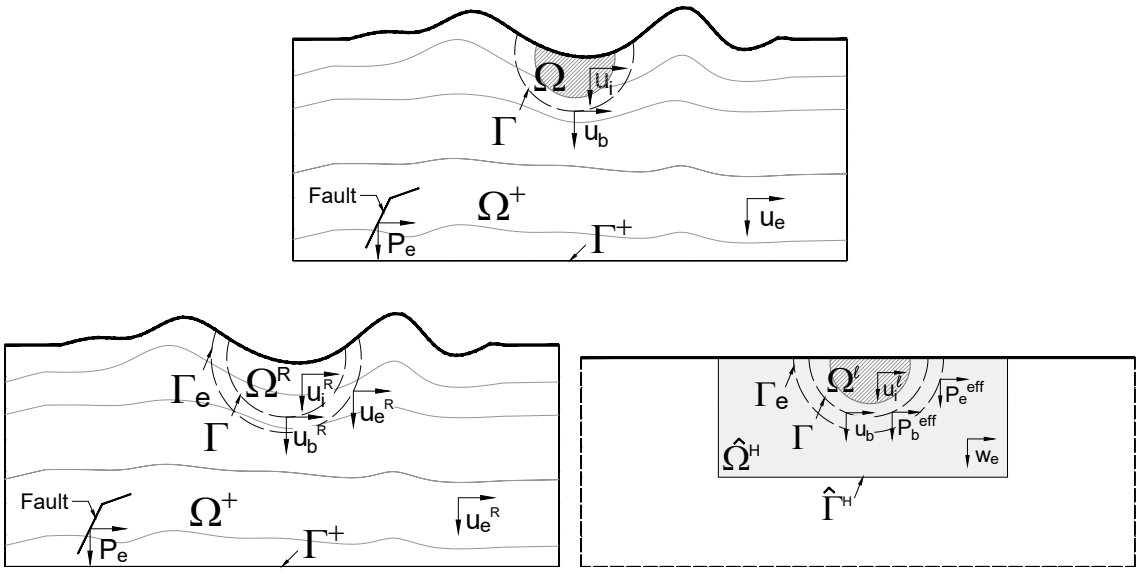

Figure 5: Generalized partition of the total domain and its related fields in the modified version of the DRM. The supporting half-space retains surface topographic irregularities of characteristic dimensions L larger than a reference value ℓ^0 and with shear wave velocity larger than β^0. The response of the supporting half-space to the earthquake excitation is a free-field motion u^R (bottom left) to be applied as excitation to a simplified model comprising only the microzone with domain Ω^ℓ (bottom right) assumed as supported by a perfect half-space with domain $\hat{\Omega}^H$

The equations of motion for the full problem correspond to;

$$\begin{bmatrix} M_{ii}^{\Omega} & M_{ib}^{\Omega} & 0 \\ M_{bi}^{\Omega} & M_{bb}^{\Omega}+M_{bb}^{\Omega^+} & M_{be}^{\Omega^+} \\ 0 & M_{eb}^{\Omega^+} & M_{ee}^{\Omega^+} \end{bmatrix} \begin{Bmatrix} \ddot{u}_i \\ \ddot{u}_b \\ \ddot{u}_e \end{Bmatrix} + \begin{bmatrix} K_{ii}^{\Omega} & K_{ib}^{\Omega} & 0 \\ K_{bi}^{\Omega} & K_{bb}^{\Omega}+K_{bb}^{\Omega^+} & K_{be}^{\Omega^+} \\ 0 & K_{eb}^{\Omega^+} & K_{ee}^{\Omega^+} \end{bmatrix} \begin{Bmatrix} u_i \\ u_b \\ u_e \end{Bmatrix} = \begin{Bmatrix} 0 \\ 0 \\ P_e \end{Bmatrix} \tag{15}$$

which are the same as in the original algorithm. However in the modified version the generalized free field may be considered representative of an auxiliary problem that includes large scale topography. This regional free-field u^R would be governed by;

$$\begin{bmatrix} M_{bb}^{\Omega^+} & M_{be}^{\Omega^+} \\ M_{eb}^{\Omega^+} & M_{ee}^{\Omega^+} \end{bmatrix} \begin{Bmatrix} \ddot{u}_b^R \\ \ddot{u}_e^R \end{Bmatrix} + \begin{bmatrix} K_{bb}^{\Omega^+} & K_{be}^{\Omega^+} \\ K_{eb}^{\Omega^+} & K_{ee}^{\Omega^+} \end{bmatrix} \begin{Bmatrix} u_b^R \\ u_e^R \end{Bmatrix} = \begin{Bmatrix} -P_b^R \\ P_e \end{Bmatrix}. \tag{16}$$

leading to seismic forces of the form;

$$P_e = M_{eb}^{\Omega^+}\ddot{u}_b^R + M_{ee}^{\Omega^+}\ddot{u}_e^R + K_{eb}^{\Omega^+}u_b^R + K_{ee}^{\Omega^+}u_e^R \tag{17}$$

The regional field u^R, and its consistent forces P_e, are expected to contain all the relevant information about the large scale topography. However, since this field was derived after removing the small-scale topography their corresponding interaction is fully neglected.

In the second step within the modified approach we construct a numerical model of the microzone with domain Ω^{ℓ} and supported by a half-space $\hat{\Omega}^{H}$, where the H superscript indicates that the half-space is an homogenized version of the actual half-space Ω^{+}. If the seismic forces given by eq. (17) are applied to this domain, the governing equations take the form:

$$\begin{bmatrix} M_{ii}^{\Omega^{\ell}} & M_{ib}^{\Omega^{\ell}} & 0 \\ M_{bi}^{\Omega^{\ell}} & M_{bb}^{\Omega^{\ell}} + M_{bb}^{\hat{\Omega}^{H}} & M_{be}^{\hat{\Omega}^{H}} \\ 0 & M_{eb}^{\hat{\Omega}^{H}} & M_{ee}^{\hat{\Omega}^{H}} \end{bmatrix} \begin{Bmatrix} \ddot{u}_i^{\ell} \\ \ddot{u}_b^{\ell} \\ \ddot{u}_e^{\ell} \end{Bmatrix} + \begin{bmatrix} K_{ii}^{\Omega^{\ell}} & K_{ib}^{\Omega^{\ell}} & 0 \\ K_{bi}^{\Omega^{\ell}} & K_{bb}^{\Omega^{\ell}} + K_{bb}^{\hat{\Omega}^{H}} & K_{be}^{\hat{\Omega}^{H}} \\ 0 & K_{eb}^{\hat{\Omega}^{H}} & K_{ee}^{\hat{\Omega}^{H}} \end{bmatrix} \begin{Bmatrix} u_i^{\ell} \\ u_b^{\ell} \\ u_e^{\ell} \end{Bmatrix} = \begin{Bmatrix} 0 \\ 0 \\ M_{eb}^{\Omega^{+}} \ddot{u}_b^R + M_{ee}^{\Omega^{+}} \ddot{u}_e^R + K_{eb}^{\Omega^{+}} u_b^R + K_{ee}^{\Omega^{+}} u_e^R \end{Bmatrix}. \tag{18}$$

Now, we further assume that the total field inside $\hat{\Omega}^{H}$ can be written like (see the bottom right in fig. 5);

$$u_e = u_e^R + w_e \tag{19}$$

which gives

$$\begin{bmatrix} M_{ii}^{\Omega^{\ell}} & M_{ib}^{\Omega^{\ell}} & 0 \\ M_{bi}^{\Omega^{\ell}} & M_{bb}^{\Omega^{\ell}} + M_{bb}^{\hat{\Omega}^{H}} & M_{be}^{\hat{\Omega}^{H}} \\ 0 & M_{eb}^{\hat{\Omega}^{H}} & M_{ee}^{\hat{\Omega}^{H}} \end{bmatrix} \begin{Bmatrix} \ddot{u}_i^{\ell} \\ \ddot{u}_b^{\ell} \\ \ddot{w}_e^{\ell} \end{Bmatrix} + \begin{bmatrix} K_{ii}^{\Omega^{\ell}} & K_{ib}^{\Omega^{\ell}} & 0 \\ K_{bi}^{\Omega^{\ell}} & K_{bb}^{\Omega^{\ell}} + K_{bb}^{\hat{\Omega}^{H}} & K_{be}^{\hat{\Omega}^{H}} \\ 0 & K_{eb}^{\hat{\Omega}^{H}} & K_{ee}^{\hat{\Omega}^{H}} \end{bmatrix} \begin{Bmatrix} u_i^{\ell} \\ u_b^{\ell} \\ w_e^{\ell} \end{Bmatrix} = \begin{Bmatrix} 0 \\ -M_{be}^{\hat{\Omega}^{H}} \ddot{u}_b^R - K_{be}^{\hat{\Omega}^{H}} u_e^R \\ M_{eb}^{\Omega^{+}} \ddot{u}_b^R + M_{ee}^{\Omega^{+}} \ddot{u}_e^R + K_{eb}^{\Omega^{+}} u_b^R + K_{ee}^{\Omega^{+}} u_e^R - M_{ee}^{\hat{\Omega}^{H}} \ddot{u}_e^R - K_{ee}^{\hat{\Omega}^{H}} u_e^R \end{Bmatrix} \tag{20}$$

where we identify as effective loads;

$$P^{eff} = \begin{Bmatrix} 0 \\ -M_{be}^{\hat{\Omega}^{H}} \ddot{u}_b^R - K_{be}^{\hat{\Omega}^{H}} u_e^R \\ M_{eb}^{\Omega^{+}} \ddot{u}_b^R + M_{ee}^{\Omega^{+}} \ddot{u}_e^R + K_{eb}^{\Omega^{+}} u_b^R + K_{ee}^{\Omega^{+}} u_e^R - M_{ee}^{\hat{\Omega}^{H}} \ddot{u}_e^R - K_{ee}^{\hat{\Omega}^{H}} u_e^R \end{Bmatrix}. \tag{21}$$

However, in our actual implementation we use for effective loads those obtained like if the full original problem was in fact the one given by the local domain supported over the homogenized half-space and corresponding to;

$$\hat{P}^{eff} = \begin{Bmatrix} 0 \\ -M_{be}^{\hat{\Omega}^{H}} \ddot{u}_e^R - K_{be}^{\hat{\Omega}^{H}} \ddot{u}_e^R \\ M_{eb}^{\hat{\Omega}^{H}} \ddot{u}_b^R + K_{eb}^{\hat{\Omega}^{H}} \ddot{u}_b^R \end{Bmatrix}. \tag{22}$$

Clearly P^{eff} and $\hat{P}^{eff}$ would be equal if $M_{ee}^{\Omega^+} \equiv M_{ee}^{\hat{\Omega}^H}$ and $K_{ee}^{\Omega^+} \equiv K_{ee}^{\hat{\Omega}^H}$.

From eq. (22) it becomes evident that two approximations violating the original hypothesis behind the DRM technique have been introduced. First, the background material has been homogenized in the reduced domain since Ω^+ has been replaced by $\hat{\Omega}^H$ and second, all the interaction between the small-scale and large-scale topography has been neglected with the main effect being considered in the regional field u^R.

The complete modified DRM technique can be summarized as follows:

- In step-I the regional displacement field at the microzone where SRA is to be conducted is obtained after consulting a database of results from a large scale simulation or from instrumental data properly filtered through a regional model. This filtering process can be conducted for a simple regional domain that can be solved at moderate computational resources.

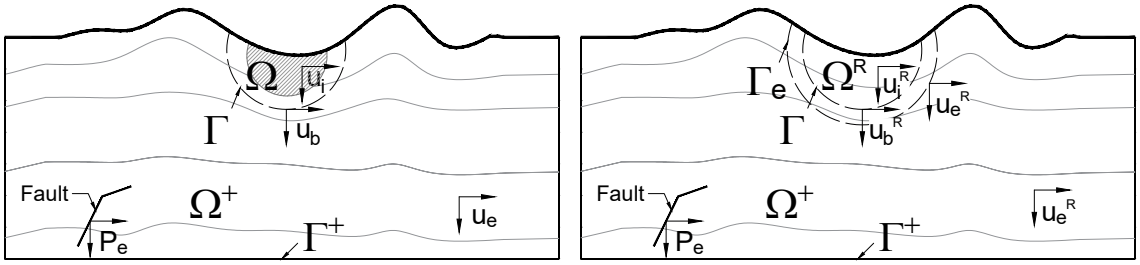

Figure 6: In step I of the m-DRM algorithm the original domain $\Omega^+ \cup \Omega$ (left) is replaced by a simplified domain (right) that can be solved at moderate computational resources after removing all the information according to predefined critical values ℓ^0 and β^0. The regional free field u^R resulting from this analysis can alternatively be obtained from analytical methods or instrumental data.

- In step-II a finite element model of the microzone supported by a homogenized version of the regional half-space is created using any commercial software with capabilities to perform dynamic analysis under time varying point loads.

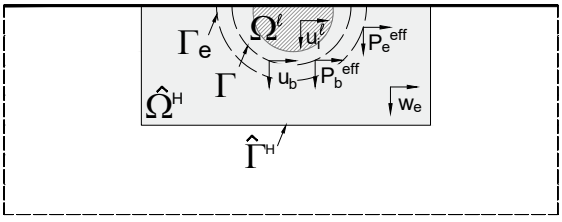

Figure 7: Reduced domain in the modified DRM algorithm. Notice that the microzone is now supported by a homogeneous half-space

The elemental matrices for this system are those in eq. (18). The mass and stiffness

coefficients from the strip of 1-element width near the microzone and matching the points of the regional field obtained in step-I are used to compute effective seismic loads like;

$$\hat{P}^{eff} = \left\{ \begin{array}{c} 0 \\ -M_{be}^{\hat{\Omega}^H} \ddot{u}_e^R - K_{be}^{\hat{\Omega}^H} \ddot{u}_e^R \\ M_{eb}^{\hat{\Omega}^H} \ddot{u}_b^R + K_{eb}^{\hat{\Omega}^H} \ddot{u}_b^R \end{array} \right\}. \tag{23}$$

This local model can take into account high resolution details of the small-scale topography and the analysis can be performed using computing resources typically available at a consulting office.

IMPLEMENTATION IN COMMERCIAL FINITE ELEMENT ANALYSIS SOFTWARE

In order to conduct step-II of the modified DRM technique we have implemented an in-house code named PIRO, which interacts with the commercial tool where SRA is to be conducted. PIRO consults the commercial software for the mesh points corresponding to the strip of elements surrounding the microzone. This information together with the regional field is used to compute effective seismic sources which are applied to the commercial tool.

The steps required in the implementation of the DRM in commercial finite element analysis software are described in fig. 8 and explained in this section.

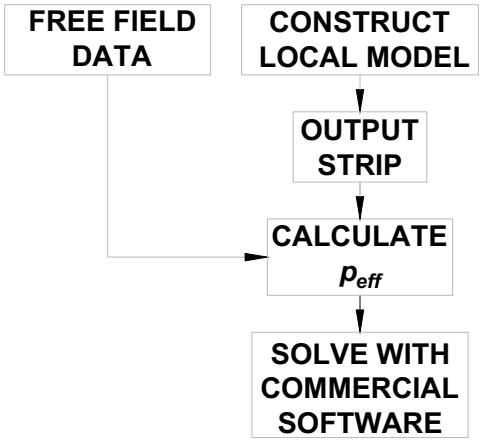

Figure 8: Main steps in the implementation of the m-DRM algorithm in commercial finite element analysis codes. It is assumed that the regional data is available from an independent step which is not the subject of this study. The local model is created in the commercial package while the effective loads are computed with the in-house software PIRO.

- Step 1. The regional displacement field u^R is extracted from a simplified model containing only the regional or large scale topography as schematized in fig. 9. This regional

information can be obtained from an existing database of results computed after a realistic simulation or from data consistent with probabilistic seismic hazard analysis methods for the zone of interest. In the current implementation this regional database is stored in a data file (regional.inp) containing time histories for displacements and the coordinates of the different points. This step is described in fig. 9 where the crossed circles represent the points for which the regional field is available.

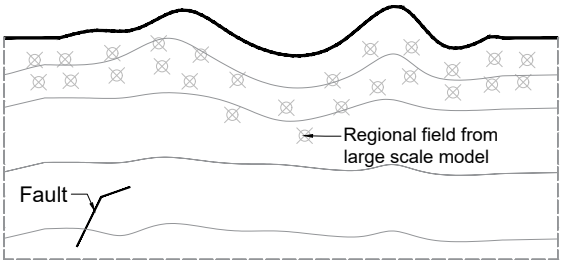

Figure 9: Schematic description of the large scale model and the corresponding regional field data. This field could be obtained with information from PSHA-USHRS, field records or simplified numerical techniques. In this work all the regional data has been produced with a BEM algorithm.

- Step 2. The homogenized local model is built using the selected commercial software. This model must specify the set of elements conforming the strip enclosing the microzone as shown in fig. 10. The mesh corresponding to the strip elements is stored into an additional file (strip.inp).

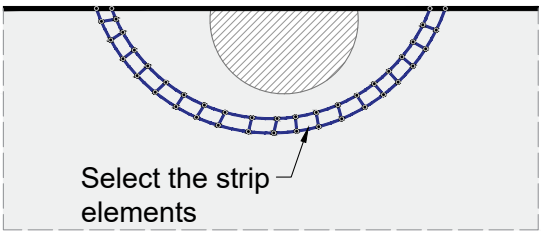

Figure 10: Description of the local model and the corresponding strip elements created with the commercial tool.

- Step 3. The effective seismic loads are obtained in a two-step process. First, the low resolution regional data u^R, stored in the file regional.inp is converted via interpolation techniques, into high resolution data in order to produce regional displacements along the nodal points in the strip as described in fig. 11.

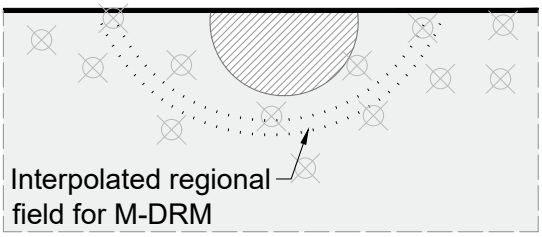

Figure 11: Representation of the interpolation step converting data of low spatial resolution into data of high spatial resolution.

The high resolution data is then used in the computation of time histories of effective loads $\hat{P}^{eff}$ making use of eq. (22). The effective loads are stored in a third file (load.inp). If the commercial software conducts time response analysis with explicit time integration algorithms using diagonalized mass matrices, this step reduces to computing only stiffness coefficients, since the mass coeffcients vanish everywhere.

- Step 4. The file containing the effective loads (load.inp) is then used as input excitation for the local model in the commercial software. In this step all the available non-linear constitutive models available in the commercial software can be activated.

Validation of the implementation

The implementation of the DRM algorithm in the in-house software PIRO together with the commercial code FEAP was benchmarked against the solution obtained with a boundary element based method. For this purpose we selected the problem of a symmetrical 30^{o} V-shaped canyon excited with vertically incident plane P, SV and SH waves. The input excitation corresponded in all cases to a Ricker wavelet of central frequency $f_c = 2.0\ Hz$. The in-plane problems were solved using full-space Green's functions while the anti-plane problem was solved with half-space Green's functions. Table 1 and 2 summarizes the parameters used in the different models. The finite element analysis was conducted using 9-noded quadrilateral elements.

Parameter	PIRO	BEM
d_t	0.00125	0.06250
Depth	8.0	-
Width	16.0	68.0
Element size	0.0250	0.0116
Number of elements	253,028	5,878
Number of nodes	1,014,045	-
Number of DOF	2,028,090	11,756

Table 1: Parameters used in the transparency tests conducted to validate the implemented computational framework for in plane problems.

Parameter	PIRO	BEM
d_t	0.00250	0.06250
Depth	8.0	-
Width	16.0	2.0
Element size	0.0250	0.0125
Number of elements	259,341	186
Number of nodes	1,039,301	-
Number of DOF	1,039,301	186
Observation points	-	1,114

Table 2: Parameters used in the transparency tests conducted to validate the implemented computational framework for anti-plane problems.

It must be pointed out that in this transparency test, where scattering of waves occur by the presence of the single V-shaped canyon there is no practical difference between the original and the modified DRM algorithm. Moreover, the test is conducted as a verification exercise of the correctness of the actual implementation of the method.

In order to assemble the vector of effective forces given in eq. (22), we used as input displacements those obtained in closed form for the case of plane P, SV and SH waves incident against the free surface of the half-space. The following material properties were used: Poisson's ratio $\nu = 1/3$, mass density $\rho = 1.0$ and P wave propagation velocity $\alpha = 2.0$. Figure 12 shows a zoom-in of the used finite element mesh. It should be noticed that the extension of the BEM mesh over each side of the scatterer is approximately twice the finite element mesh. This is necessary since for the in-plane problems we are using full space Green's functions. However, this is not the case in the anti-plane problem.

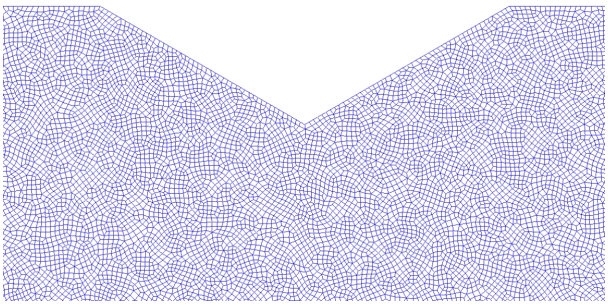

Figure 12: Zoomed view of the FEM mesh used for the transparency test conducted over the V-shaped canyon

Figure 13 to fig. 18 display time histories of the displacement field computed with the implemented finite element framework and a boundary element algorithm for a set of receivers located over the free surface of the domain. For the in-plane problems the results correspond to the horizontal and vertical displacement field, while in the case of *SH* waves we display the corresponding anti-plane motions. In each case the left column corresponds to the FEM displacement solution and the right column to the BEM solution. For comparison purposes maximum values of the displacement amplitude obtained with each method are also provided. The spurious waves originating at the exterior receivers in the finite element models are due to the absence of absorbing boundaries in the finite element simulations. In this particular problem the issue is evident at normalized locations $x/a = 7$ y $x/a = -7$ in which it is observed how the contribution from the first order diffraction initially arrives and then returns due to its artificial reflection. In the results corresponding to the anti-plane problem this spurious field is less important and it is hardly visible in the synthetic seismograms. Although absorbing boundaries are important to produce a robust wave propagation software, it must be considered that in the DRM algorithm the problem for the exterior domain is formulated in terms of relative or scattered motions, instead of total displacements, and as a result, these spurious reflections at the exterior boundary are of smaller amplitude. However, in all the subsequent analysis presented in this work the domain is of an extension large enough as to produce a workable time window free of spurious reflections.

A second difference in the results from both methods is observed for the maximum displacements at the corners of the canyon (points $x/a = 1$ y $x/a = -1$). This is due to the fact that in the BEM discretization we are using constant field elements and the canyon apex is not a BEM node which introduces some inaccuracies in the BEM results, while in the FEM model the effect of these diffraction sources is explicitly included in the model.

As a final result and with the idea of having a physical validation we also obtained snapshots of the propagation patterns over the full domain computed with the finite element method (see fig. 14, fig. 16 and fig. 18). The snapshots in the right panel in each figure shows the time instant in which the plane wave hots the free surface of the canyon, while the right panel shows how

the diffracted waves start to rebuild the plane front as the wave moves away from the scatterer.

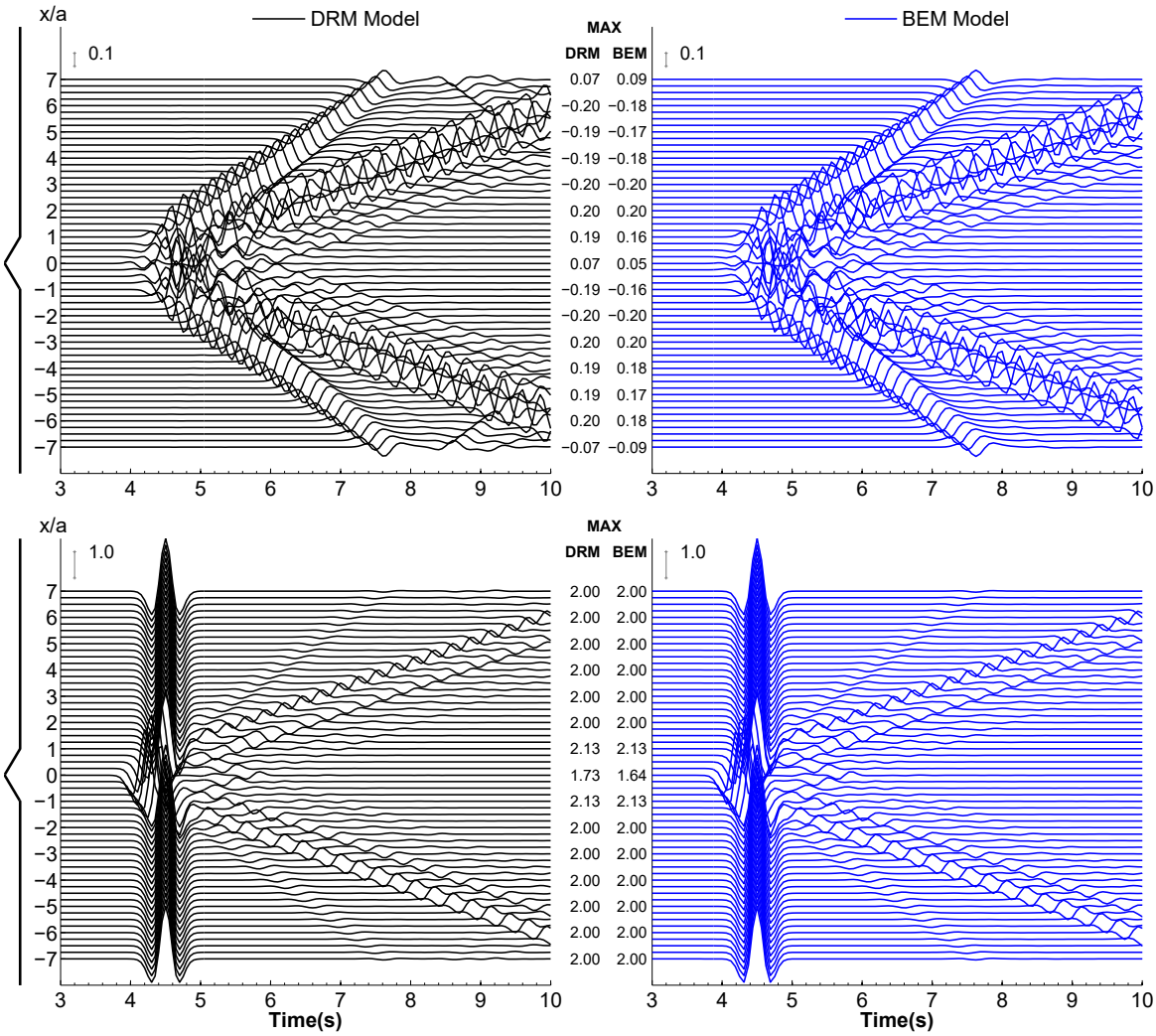

Figure 13: Synthetic seismograms for the horizontal (top) and vertical (bottom) displacement components for a set of receivers located over the free-surface of the V-shaped canyon submitted to a vertically incident P-wave computed with the DRM approach (left) and the BEM algorithm (right).

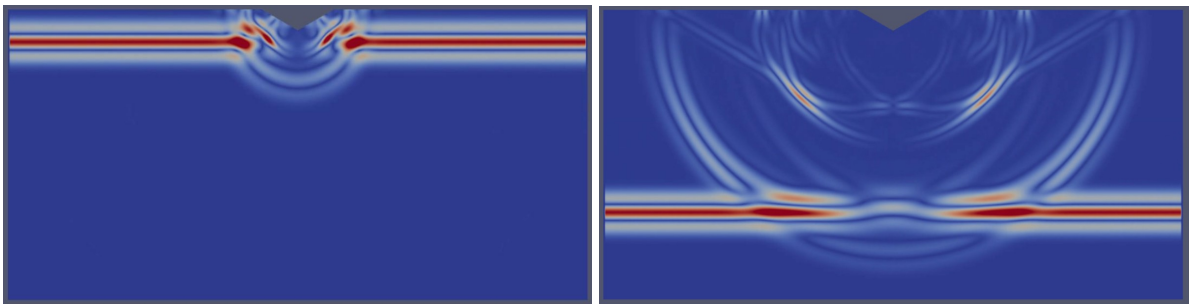

Figure 14: Snapshots of the propagation patterns for the total amplitude of the displacement field due to a P-wave obtained with the implementation of the DRM approach.

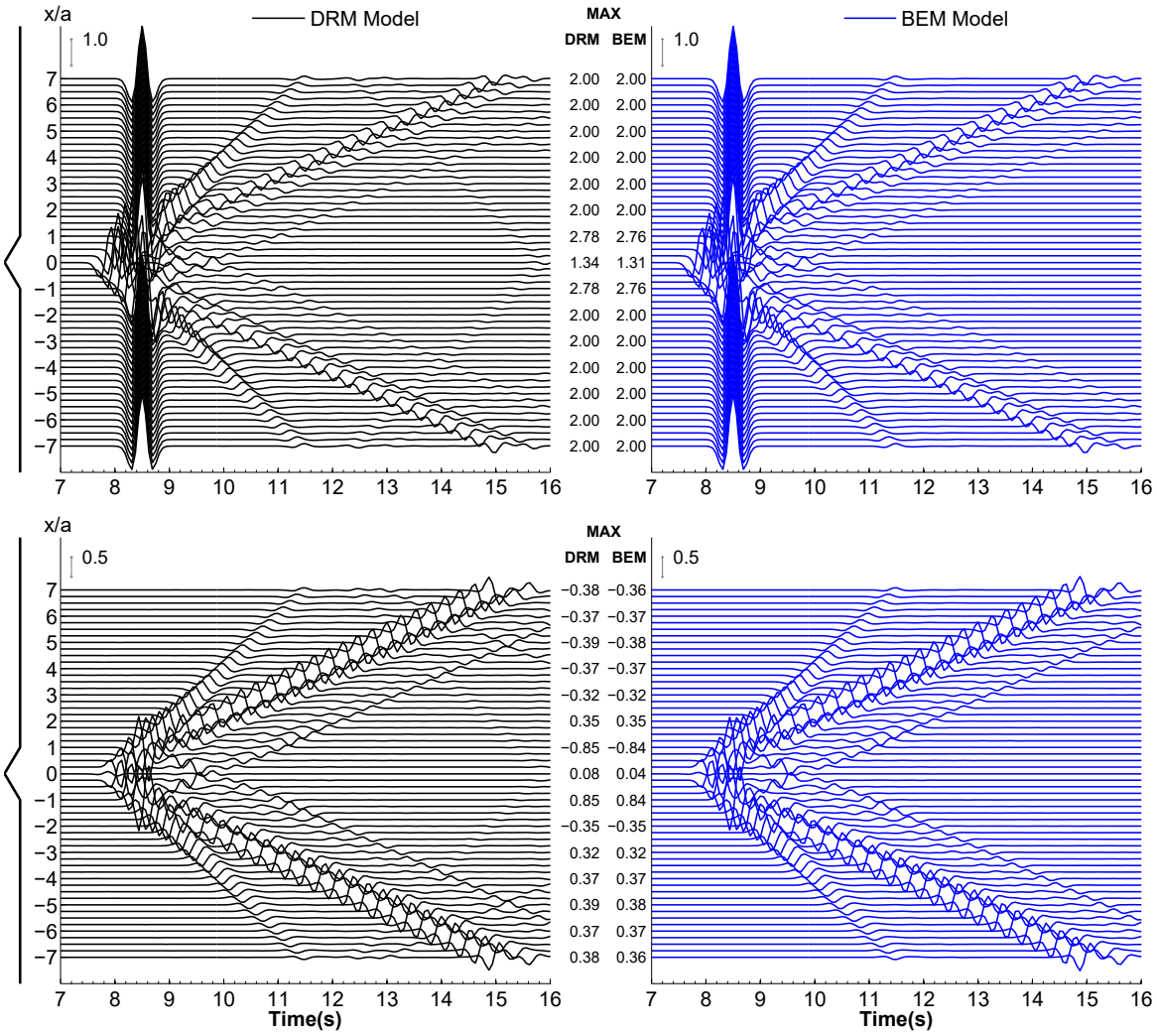

Figure 15: Synthetic seismograms for the horizontal (top) and vertical (bottom) displacement components for a set of receivers located over the free-surface of the V-shaped canyon submitted to a vertically incident SV-wave computed with the DRM approach (left) and the BEM algorithm (right).

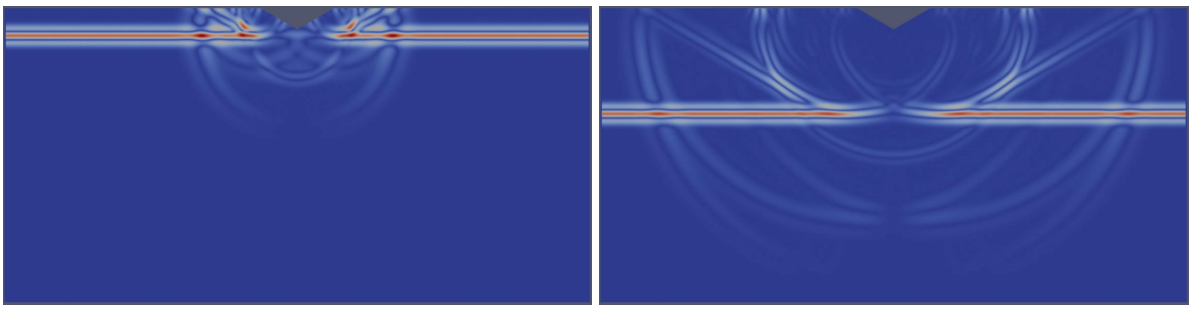

Figure 16: Snapshots of the propagation patterns for the total amplitude of the displacement field due to a SV-wave obtained with the implementation of the DRM approach.

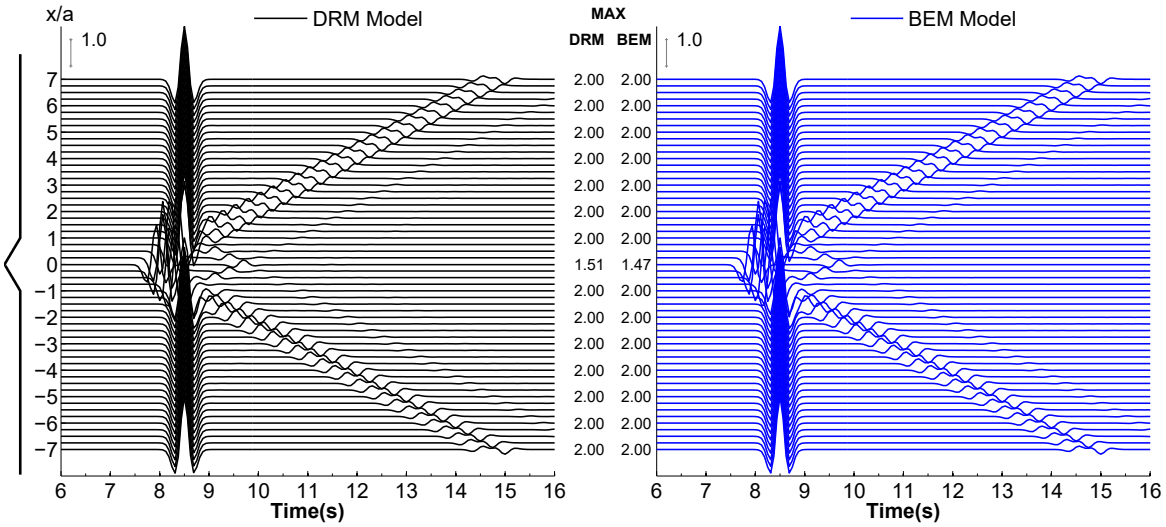

Figure 17: Synthetic seismograms for the anti-plane displacement component for a set of receivers located over the free-surface of the V-shaped canyon submitted to a vertically incident SH-wave computed with the DRM approach (left) and the BEM algorithm (right).

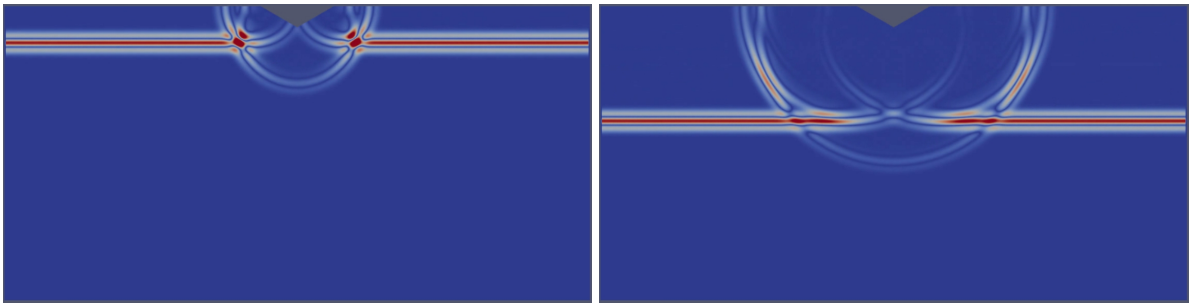

Figure 18: Snapshots of the propagation patterns of the anti-plane field due to a SH-wave obtained with the implementation of the DRM approach.

VALIDATION OF THE MODIFIED DRM METHOD

Since the purpose of the current study is to assess the capabilities of the proposed modified DRM algorithm to predict the response of seismic scenarios comprising strong contrasts due to the simultaneous presence of large and small scale topographic irregularities and by hard and soft material properties, we have selected as study case the idealized problem of a 60^0 V-shaped canyon (representing the regional feature), combined with a microzone in the form of a semi-circular canyon and a valley. The geometric parameters defining the 60^0 V-shaped canyon are shown in fig. 19. In this case the characteristic regional scale L corresponds to the half-width a. In the current analysis the incidence angle has a value $\alpha = 0^0$ and the half-space has a shear wave propagation velocity c.

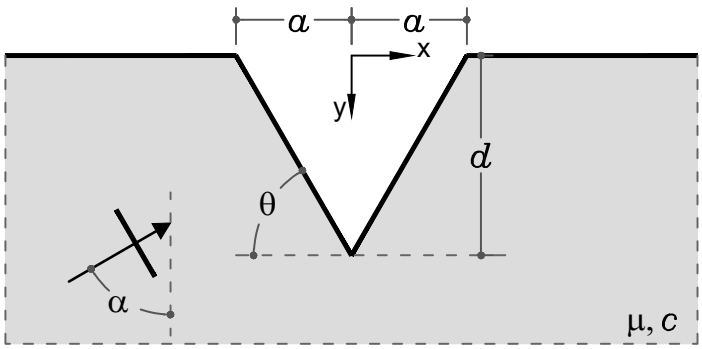

Figure 19: Regional topography defined by a 60° V-shaped canyon.

To gain a conceptual understanding of the canyon response, the problem is first analyzed with the superposition based diffraction (SBD) technique formulated by Jaramillo et al. (2013). That technique splits the solution into the displacement components induced by the optical field and those contributed by the diffracted field. As will be shown next, the ray theory analysis based on the SBD technique reveals that this particular configuration produces a strong regional effect in the zones adjacent to the canyon.

Ray theory solution for the 60° V-shaped canyon

We conducted frequency domain analysis using an in-house software based on the direct boundary element method. The code uses a half-space Green's functions satisfying the radiation boundary condition. All the results are described in terms of the dimensionless frequency

$$\eta = \frac{2af}{c} = \frac{\omega a}{\pi c} = \frac{\kappa a}{\pi} = \frac{2a}{\lambda} \tag{24}$$

where f =frequency in Hz, ω =circular frequency, κ =wave number, λ =wave length and c = wave propagation velocity.

In order to study the regional topographic effect introduced by the canyon, we separate the field into a frequency independent part (the optical field), and a frequency dependent part (the diffracted field). This approach is described in Jaramillo et al. (2013) who use it to build the solution to the scattering of SH waves by a surface topography of arbitrary shape and in Gomez et al. (2013) who also separated the fields in the study of a semi-circular and a rectangular canyon under incident P and SV waves. Such partition is given by;

$$u^T = u^{IN} + u_F^R + u^D \equiv u_F^0 + u^D \tag{25}$$

where u^{IN} = incident field, u_F^R = field reflected over the free surface of the irregularity and u^D = diffracted (frequency dependent) field. In eq. (25), the frequency independent contribution, corresponding to the optical field and resulting from the superposition of the incident and reflected rays $u^{IN} + u_F^R \equiv u_F^0$ is named the physical incoming motion. In this work we compute u^T numerically using a BEM algorithm while u_F^0 is obtained analytically using classical ray theory. The frequency dependent term u^D is then simply obtained from eq. (26) according to;

$$u^D = u^T - u_F^0. \tag{26}$$

Here we first obtained the model response for independent harmonics of unit amplitude and frequency f. Figure 20 depicts the ray theory solution. Each arrow indicates whether a ray is an incident or a reflected ray, while the dashed lines separate zones of existence of different numbers of rays. The right part of the figure displays the maximum value in the amplitude of the transfer function for the optical field along the canyon surface.

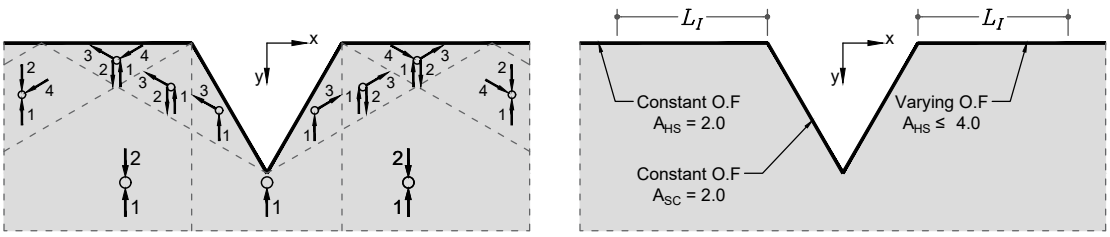

Figure 20: Separation of the total domain into subdomains according to regions of existence of incident and reflected rays. The number of rays gives maximum expected values of the amplitude of the optical field. The finite zone L_I adjacent to each side of the canyon corresponds to a region of enlarged optical field.

Of special relevance is the zone of extension L_I adjacent to each side of the canyon where the optical field may reach an amplitude of 4.0. Hereafter this zone is referred to like the illuminated zone and its extension is given by;

$$L_I = \frac{d}{tan(2\theta - \pi/2)} - a. \tag{27}$$

The illuminated zone is precisely the location where the large scale regional effect has its major impact over a localized small scale topographic feature (to be added later to the model).

Figure 21 shows the frequency domain transfer functions over the topographic surface and over the free surface of the half-space at different values of the dimensionless frequency η. Each plot contains the results corresponding to the discontinuous field u_F^0 as depicted in fig. 20, the total field u^T (computed with the boundary element algorithm) and the diffracted field u^D.

The set of rays existing in each part of the domain determines the maximum and minimum amplitude of the optical field, while its spatial variation is determined by the addition of rays with different wave vectors. In this set of frequency domain results an amplitude value of 2.0 corresponds to the half-space response.

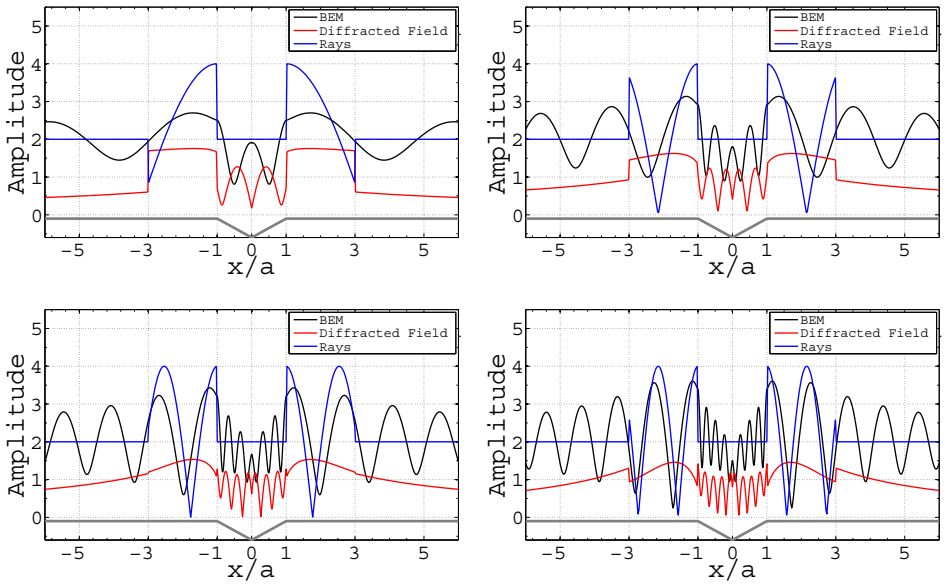

Figure 21: Frequency domain transfer function over the free surface of the $V-$shaped canyon. Each plot represents a different value of the dimensionless frequency parameter as follows $\eta = [0.5, 1.0, 1.5, 2.0]$. In order to identify the contribution from each term the total response (denoted as BEM) has been separated into optical and diffracted fields.

From the frequency domain amplitude functions it is evident that inside the canyon the response is dominated by the diffracted field, which introduces deamplifications at low frequencies and a small amplification in the high frequency regime. By contrast, in the illuminated zone adjacent to the canyon, the response is controlled by the optical field. This implies that if a small-scale topographic irregularity is placed within this zone a strong interaction between the two geometries should be expected. Such interaction corresponds to the diffraction of the primary vertically incident waves and of the rays reflected over the slopes of the V-shaped canyon and deflected to the illuminated zone. The DRM regional or free field motion defined by eq. (19) and later converted to effective loads, is expected to capture the rays focused over the illuminated zone but it should not capture the interaction between both topographies since in the current modified approach the microzone is assumed supported by a perfect half-space. This deficiency implies that the modified DRM approach should have limitations in problems with important interactions between the regional and local effect. Since the 60^0 V-shaped canyon exhibits such an important regional effect, it constitutes a good example to assess the effectiveness of the modified DRM technique.

Interaction with a localized neighbourhood topographic irregularity

In order to test our modified DRM method we now introduce a small-scale semi-circular canyon in the neighbourhood of the previously studied 60^0 V-shaped canyon as shown in fig. 22. The regional and site specific characteristic dimensions L and ℓ, correspond in this case to the width and radius of each topographic irregularity. The semi-circular canyon is located at a distance r from the V-shaped canyon. That location will be varied with respect to the illuminated zone of distance L_I as described in table 3 and depicted in fig. 23. It is convenient to introduce regional and local dimensionless frequencies $\eta = L/\lambda$ and $\gamma = \ell/\lambda$ related by the aspect ratio parameter $s = \eta/\gamma \equiv L/\ell$. Similarly introducing a third dimensionless frequency $\chi = r/\lambda$ we have the following normalized distance between canyons $d = \gamma/\chi$.

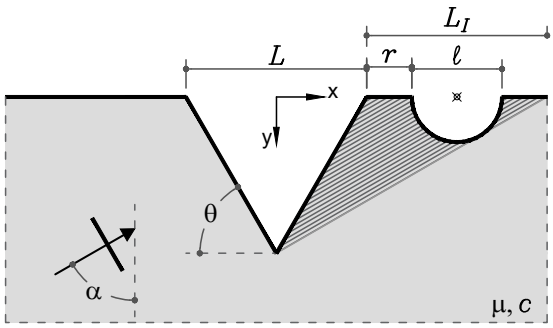

Figure 22: Semi-circular canyon resembling a localized small-scale topographic irregularity of characteristic dimension ℓ located in the vecinity of a 60° V-shaped canyon resembling a regional topography of characteristic dimension L.

Case	s	c_ℓ/c	r	
1	2.0	-	0.5	$r \in L_I$
2	2.0	-	2.0	$r \notin L_I$
3	4.0	-	0.5	$r \in L_I$
4	2.0	0.5	0.5	$r \in L_I$

Table 3: Geometric parameters defining the models used in the current study.

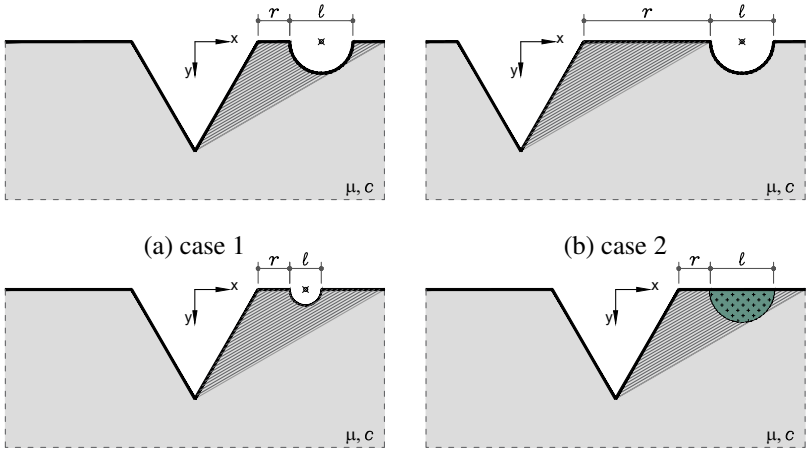

(a) case 1 (b) case 2

(c) case 3 (d) case 4

Figure 23: Location of the micro-zones with respect to the regional topography according to the 4 cases defined in table 3. The shaded area indicates the region of influence of the large-scale topography.

In this idealized scenario the regional and local topography are expected to interact through the diffractions generated by the geometric singularities at the right apex of the V-shaped canyon and the left corner of the semi-circular canyon. Both geometric singularities will diffract the primary vertically incident wave field and its reflection. Within the context of the SBD method these are referred to like first order diffractions. These first order cylindrical diffracted waves will propagate over the surface and towards the interior of the domain and towards the opposite singularity, generating further diffraction events in the form of higher order diffracted waves. On the other hand, the rays reflected over the slopped part of the V-shaped canyon and producing the illuminated zone of extension L_I (see fig. 22), will experience also diffraction by the the semi-circular canyon.

It is then clear that the regional free-field motion u^R will produce DRM-forces containing the effect of the vertically incident wave; of the rays producing the illuminated zone of size L_I; and of the primary diffraction of the V-shaped canyon. By contrast, this field would lack the second order diffraction generated by the trapping of energy between the two singularities and the first order diffraction of the rays reflected over the slopped part of the canyon.

Cases 1 and 3, reported in table 3 are for a micro-zone located at the same distance r from the regional canyon but for different aspect ratios. In both cases the semi-circular canyon is located inside the over-illuminated zone L_I. On the other hand case 2, corresponds to an aspect ratio $s = 2.0$ and assumes the micro-zone to be located out of the region of influence of the regional topographic effect. In the final model, corresponding to a semi-circular valley, we locate this micro-zone inside the over-illuminated zone L_I, providing an analysis problem with a combined geometrical-mechanical effect.

In the simulations we used the following parameters. Angle of the V-shaped canyon θ= 60°, depth d= 1.73, angle of incidence of the plane front α= 0°, shear modulus μ= 1.0, shear wave propagation velocity c= 1.0, canyon width L= 2.0. A particular set of parameters is given in table 4.

	Step 1: BEM model	**Step 2: m-DRM model**
Depth	1.73	6.85
Width	2.00	12.50
d_t	0.0250	0.0001
Time steps	1,600	15,000
Element size	0.005	0.010
No of elements	800	994,142
No of nodes	-	3,980,903
Strip elements	-	312
Loaded nodes	-	1,879

Table 4: Model parameters used in the simulation of case 1 with the m-DRM algorithm

In order to test the effectiveness of the proposed modified version of the DRM algorithm we performed a total of 4 different analysis summarized in table 5 and defined as follows: (i) a full model representing in this problem the exact response and including the regional V-shaped canyon and the micro-zone; (ii) a regional model (shown in fig. 24) containing only the V-shaped canyon and with a response giving the regional field u^R; (iii) a local model corresponding to the micro-zone submitted to the independent action of the incident plane wave and (iv) the m-DRM model (shown in fig. 25) corresponding to the application of the regional field obtained from the model given in (ii). Models (i) through (iii) were solved using the boundary element method and model (iv) was solved using the commercial code FEAP in combination with the in-house software PIRO used to computed the effective input loads.

Figure 24 and fig. 25 show the models corresponding to cases (ii) and (iv). In particular model (ii) is used during the first analysis step, where the regional field u^R is computed using the boundary element method with the mesh described by the blue line in fig. 24. Since the used BEM code uses half-space Green's functions only the canyon surface is discritized. The same figure shows by a dashed line the location of the boundary of the semi-circular canyon, while the continuous black line shows the observation points where the regional field is stored. Similarly, fig. 25 shows the mesh used in the commercial code FEAP during the application of the m-DRM algorithm. The scatterer in each case corresponds to the domain discretized by the yellow elements, while the purple elements contain the strip where the DRM effective loads are imposed.

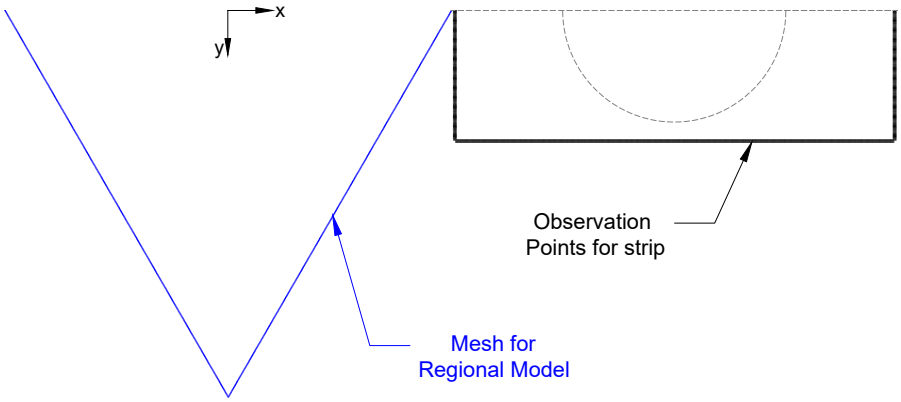

Figure 24: Complete idealized seismic scenario. The blue line shows the BEM mesh used to represent the regional model. The dashed semi-circular line depicts the boundary of the semi-circular topography and the black continuous line shows the boundary where the regional field is stored.

Model	Method	Geometry
Full	BEM	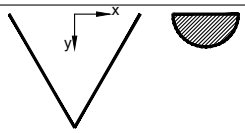
Regional	BEM	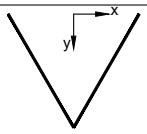
Local	BEM	
m-DRM	PIRO+FEAP	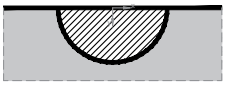

Table 5: Models and analysis method used in each of the simulations conducted in this study.

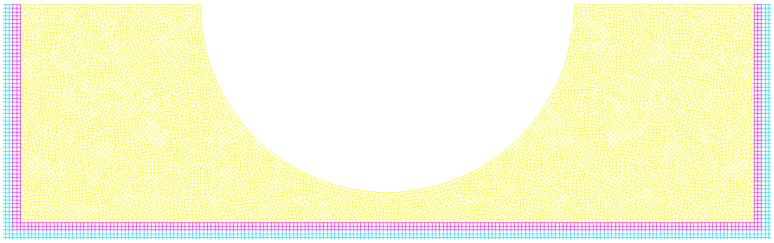

Figure 25: Finite element mesh used in the commercial code FEAP and showing the scatterer and enclosing boundary where effective forces are applied.

Figure 27 and fig. 28 show the spatial distribution of the amplitude function over the nor-

malized free surface of the micro-zone for low and high values of the dimensionless frequency $\gamma = \ell/\lambda$ respectively. As shown in each figure, the columns correspond to a different value of the frequency parameter while each row represents one of the cases defined in fig. 23. In all the cases the main plot displays the results from models (i), (iii) and (iv) while the regional field corresponding to model (iii) is given in the insert function in each case. As an aid in the interpretation of the results fig. 26 shows labels for different zones over the canyon surface. Each label describes the number of rays that hit the surface due to the incidence of the main front and to the rays reflected from the free surface of the V-shaped canyon.

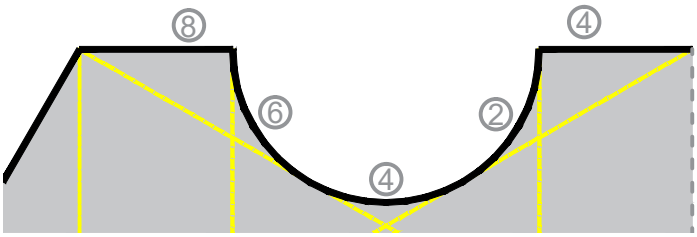

Figure 26: Maximum expected amplitude of the m-DRM optical field over the different regions of the micro-zone.

It is observed that in the right side of the micro-zone, in cases (1) and (2) for aspect ratio $s = 2.0$, the response is mainly governed by the optical field which results in the response being very close to the prediction of the local model (i.e., dashed lines) since these locations are precisely those in the shadow zone of the rays reflected from the V-shaped canyon starting at $x/\ell = 0.25$. Over the left side of the micro-zone the total field takes large values explained by the interaction, in terms of diffracted waves, between both topographic irregularities. By contrast, the results for case (3) for aspect ratio $s = 4.0$, in the right side of the micro-zone deviate from those predicted by the local model since the influence of the diffracted field produced by the regional topography is very strong over these locations. The same trend is observed in the response for case (4) corresponding to a micro-zone given by a semi-circular valley where the mechanical effect modifies not only the main incident front but also the diffracted field generated by the regional canyon. This trend is observed in the low and high frequency regime. In summary, the response in the right zone of the microzone is closely captured by the local model but is in general under-predicted over the left side where the regional topography has a stronger influence. Now, when comparing the performance of the m-DRM approach on capturing the response of the micro-zone it is evident that, at least for this idealized problem the results are in high agreement through the frequency range of interest and for all the different locations over the micro-zone.

As an additional verification of the effectiveness of the m-DRM technique we also present in fig. 29 and fig. 30 the amplitude functions throughout the frequency range of interest and at various locations over the micro-zone. The observation point is shown by the insert figure

in each case. When observed from this frequency perspective, the deviation between the local and full model is more evident. It is also observed how the m-DRM predicts the exact response with high accuracy.

In fig. 31 we also show the amplitude functions and the displacement time histories predicted by the 4 models. Of special interest are the results corresponding to case (4) where the mechanical effect is clearly observed in the results from the full and local model. It is interesting to observe that the solution in this case is similar to the prediction of a one-dimensional wave propagation analysis. This is captured by both, the local and the full model. The differences between these two sets of results are expected since the regional effect, observed in the results from the full-model, produces an enhanced incident field, which is subsequently amplified by the mechanical effect. Moreover, this effect is fully captured by the m-DRM technique which suggests that a method based on the classical one-dimensional wave propagation model but with an excitation corrected by regional effects may be a promising alternative.

In the final part of this verification study we present in fig. 32 a comparison between displacement time histories obtained with the full, local and m-DRM model. Maximum values obtained with each method are given for reference. Once again, excellent agreement between the full model and the m-DRM predictions is observed.

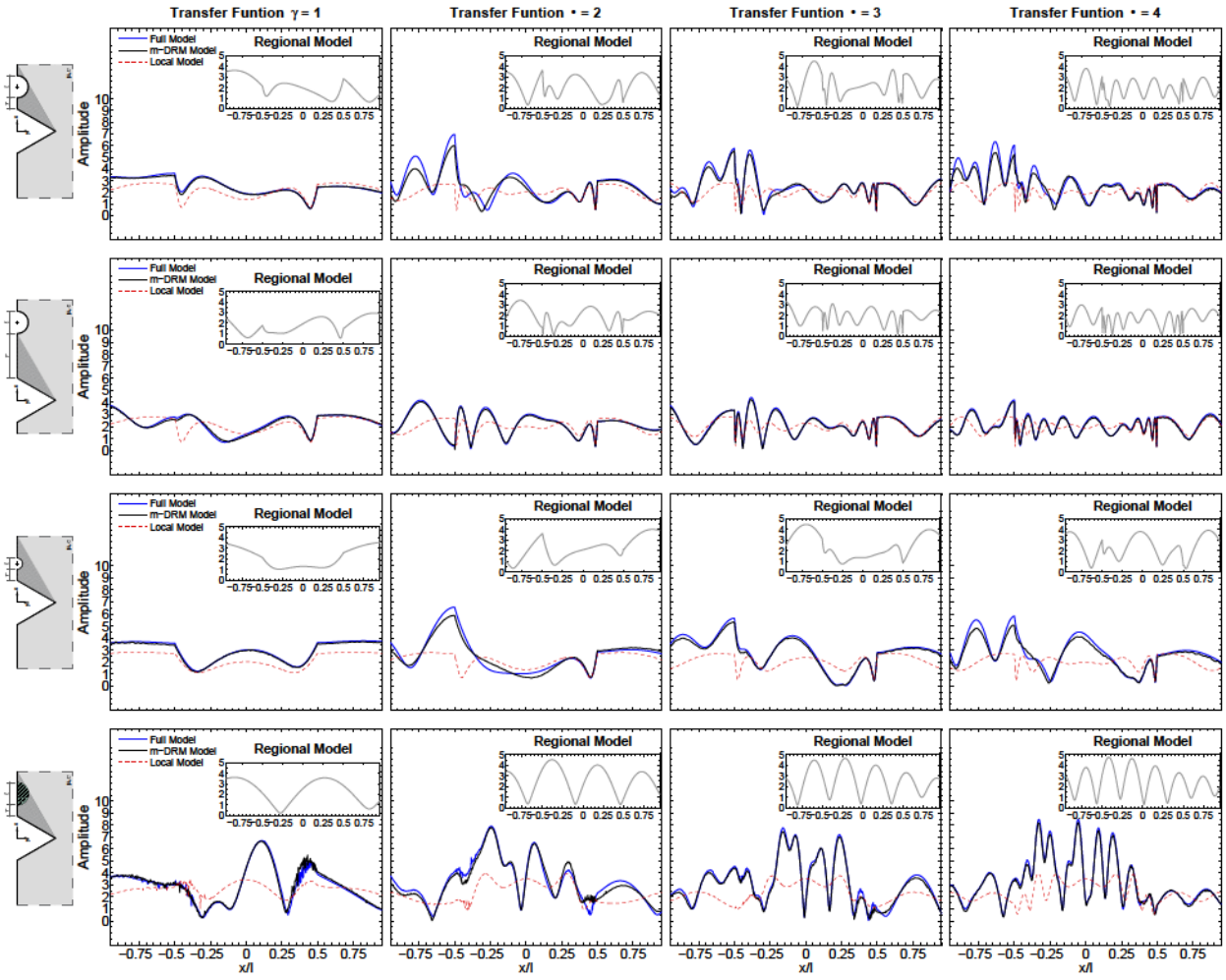

Figure 27: Frequency domain amplitude function over the normalized free surface of the semi-circular canyon for low values of the dimensionless frequency γ corresponding to [1.0, 2.0, 3.0, 4.0]. Each row of results corresponds to the cases defined in table 3.

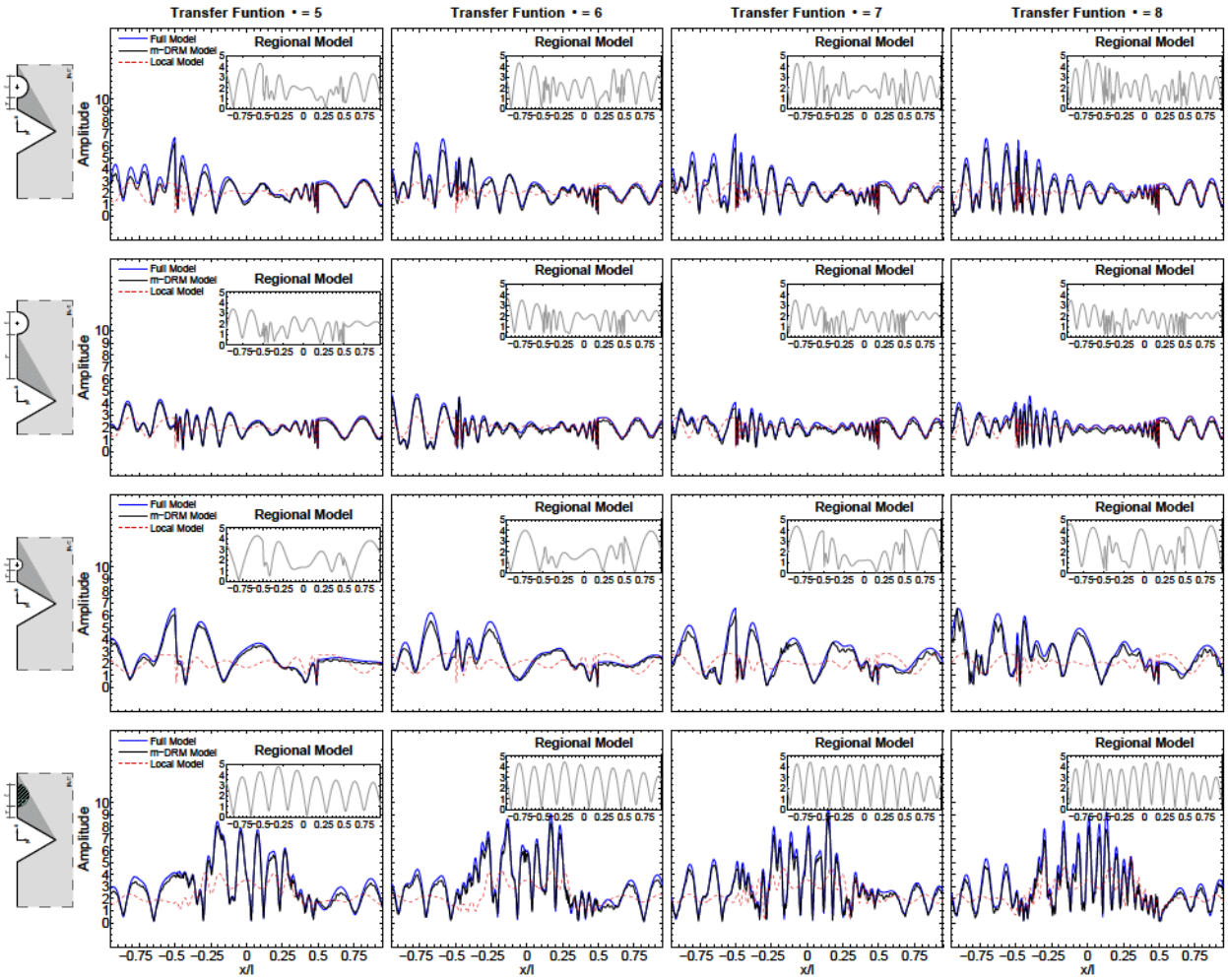

Figure 28: Frequency domain amplitude function over the normalized free surface of the semi-circular canyon for high values of the dimensionless frequency γ corresponding to [5.0, 6.0, 7.0, 8.0]. Each row of results corresponds to the cases defined in table 3.

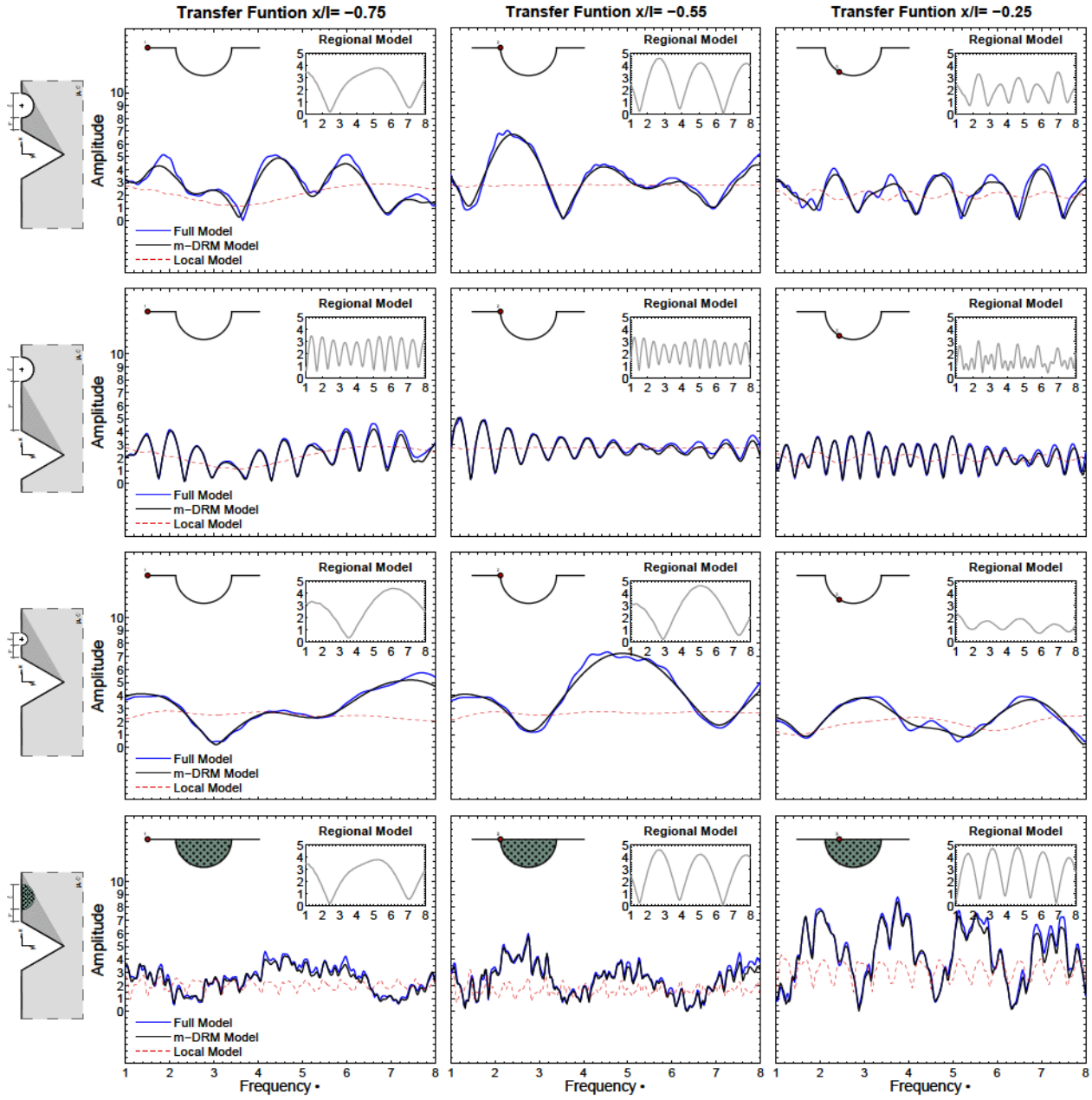

Figure 29: Frequency domain amplitude function for selected locations along the left part of the micro-zones for each one of the cases defined in table 3.

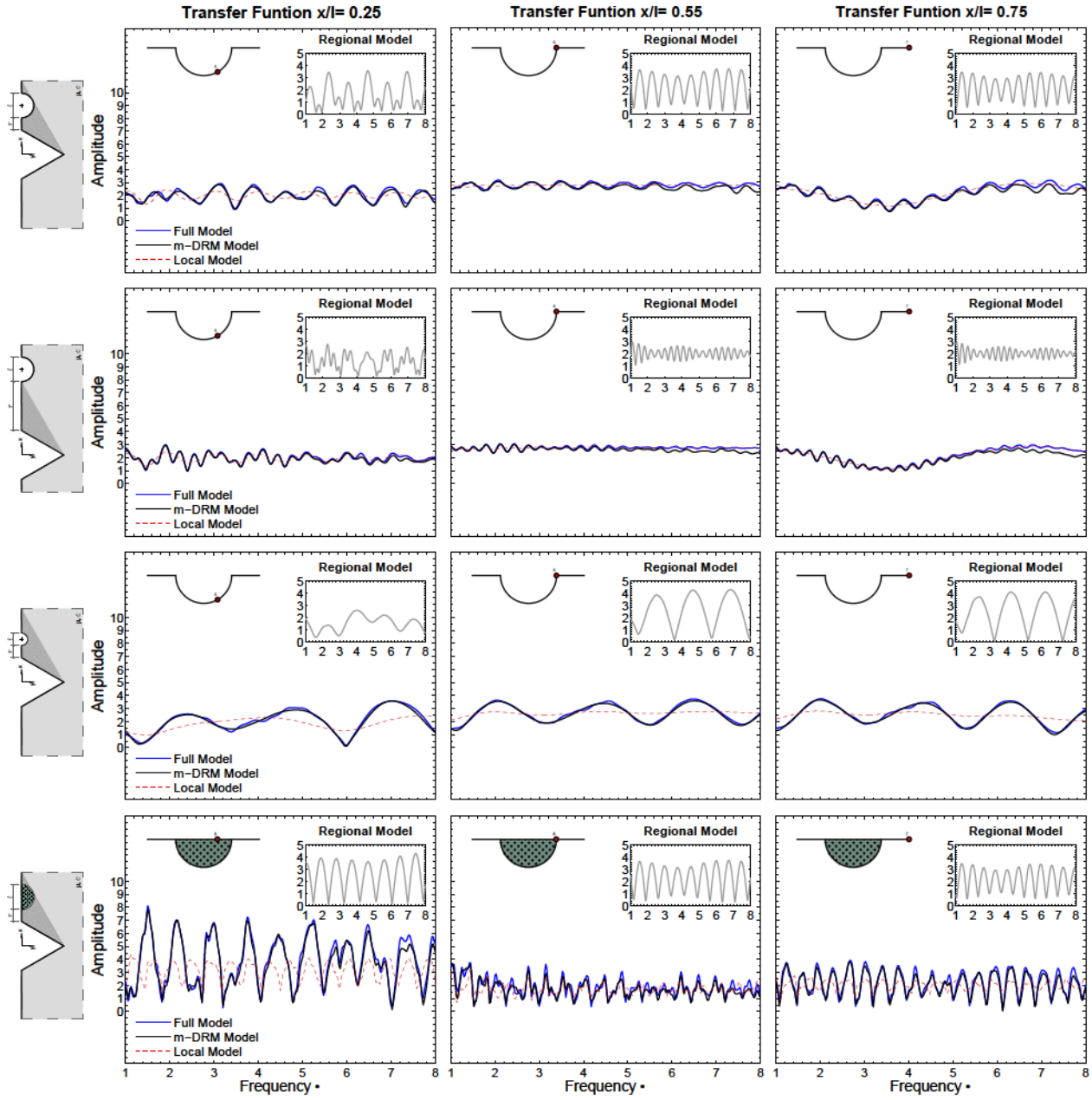

Figure 30: Frequency domain amplitude function for selected locations along the right part of the micro-zones for each one of the cases defined in table 3

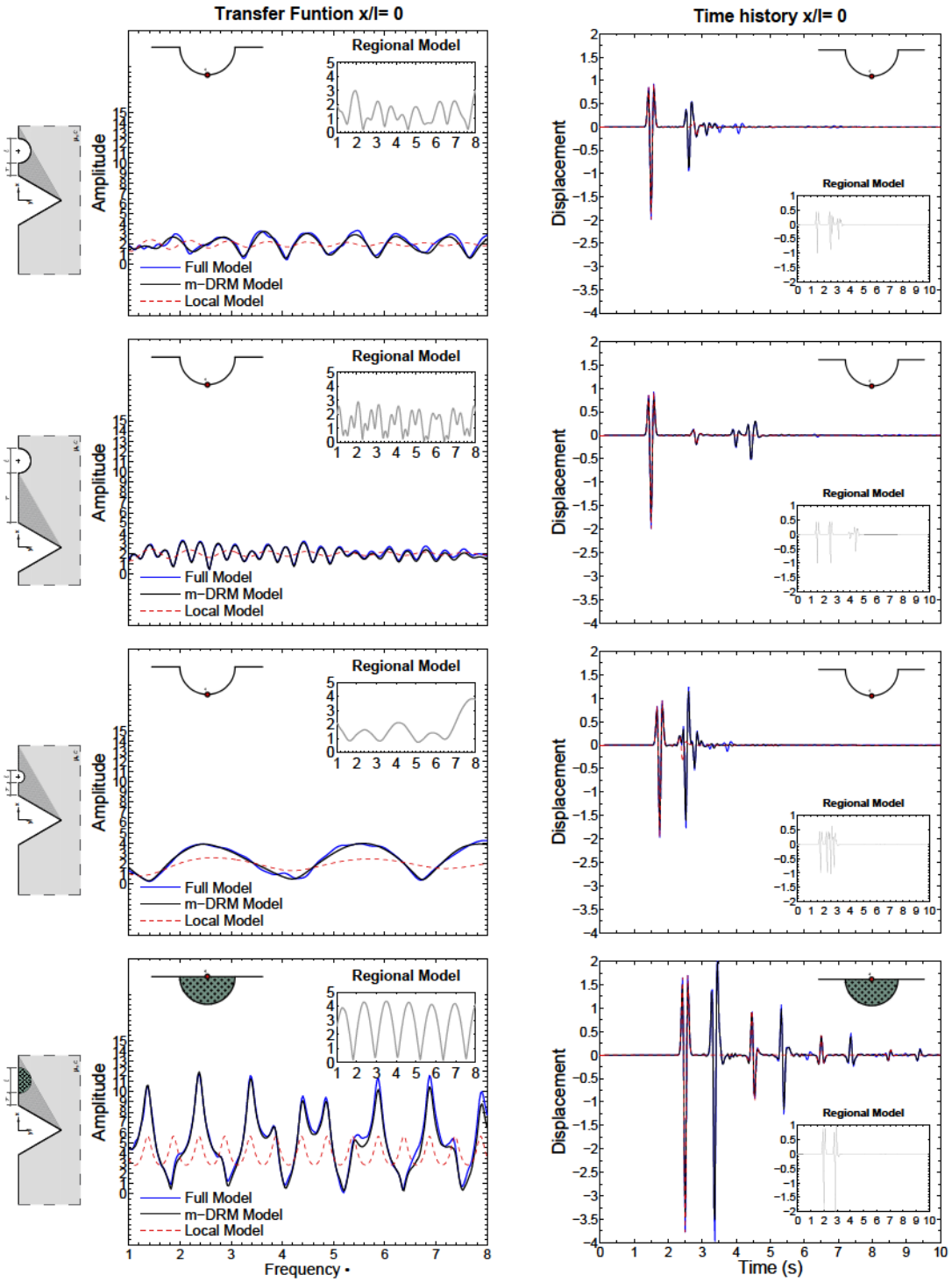

Figure 31: Fourier amplitude function and time history response corresponding to the central point of the semi-circular topography obtained with the full model, the m-DRM approach and the local model

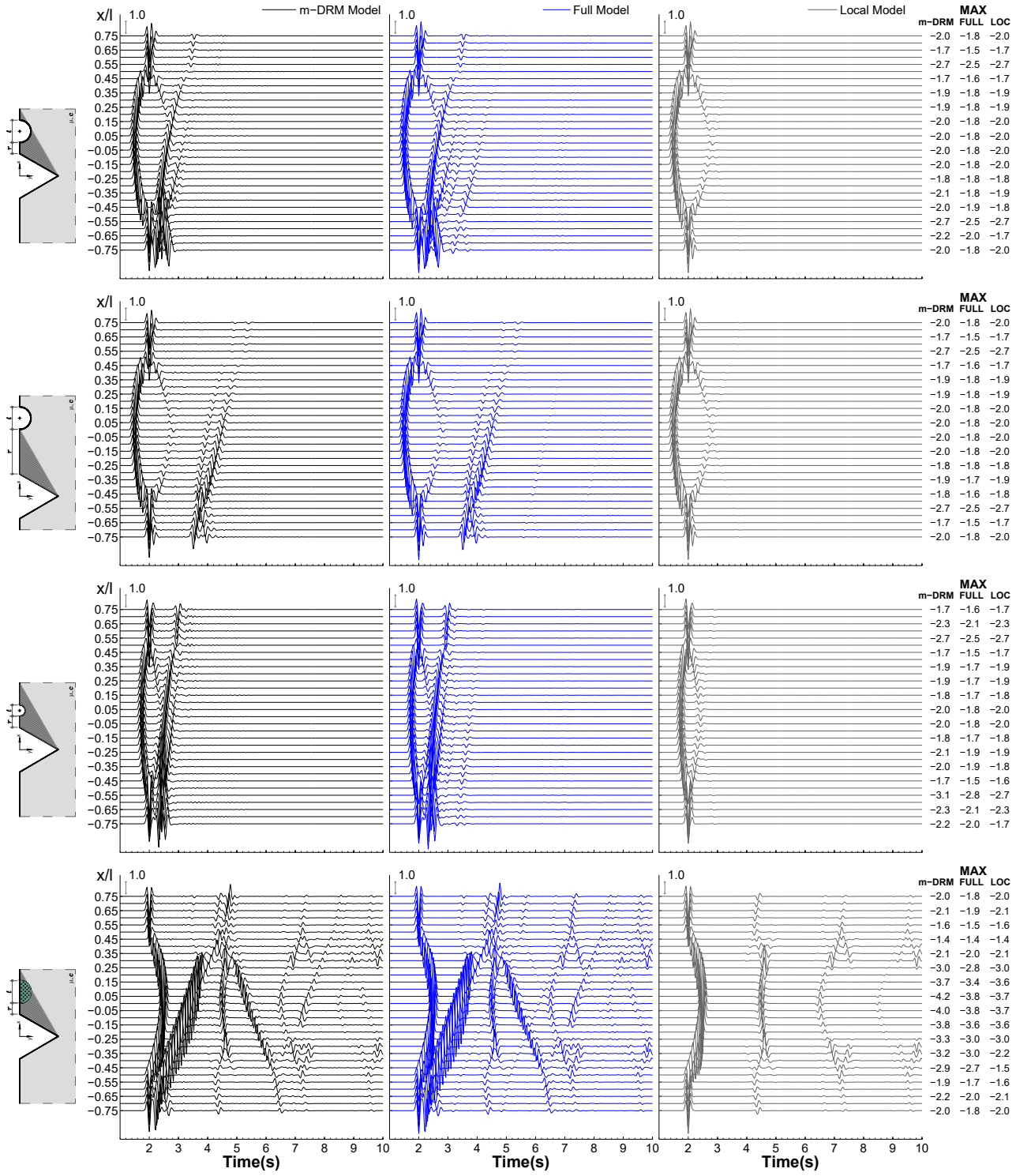

Figure 32: Synthetic seismograms for a set of receivers located over the free surface of the micro-zone computed with the m-DRM approach, the full model and the local model.

DISCUSSION

From the set of results presented above, the case of a micro-zone conformed by the semi-circular valley located inside the zone of strong influence of the regional field is highly interesting. The results for this particular case are shown in fig. 33 where we display amplitude functions for the central point of the free-surface of the valley computed with: the full-model; the local model and; the m-DRM approach. For reference we have also added the results from a one-dimensional wave propagation analysis for an equivalent one-layer system (black dashed line in the figure).

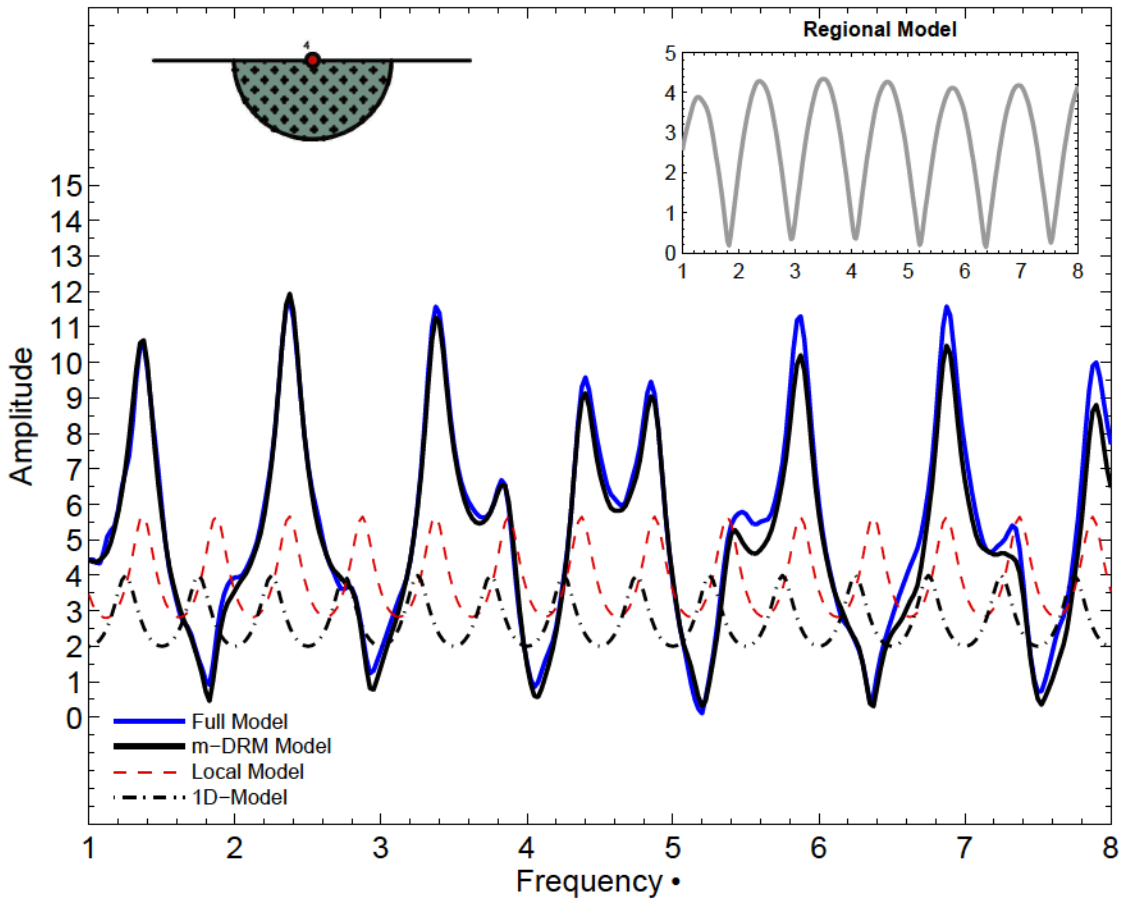

Figure 33: Amplitude functions for the central point of the semi-circular valley. The results were computed with the full model (BEM algorithm), the m-DRM model (FEM algorithm), the local model (BEM algorithm) and the equivalent one-dimensional model (analytical). The insert function correspond to the regional model and γ is the dimensionless frequency.

It is observed that the predictions from the local and 1D model (Roësset, 1970) are similar to each other, with only small differences in amplitude and phase. Interestingly, the results from the full-model conserve the same pattern of a one-dimensional model but with a much larger amplification. This may be interpreted as the result of a classical one-dimensional wave

propagation analysis but with a corrected incident field as corroborated by the accuracy of the results corresponding to the m-DRM approach. A method motivated by this DRM approach and intended to incorporate topographic effects into SRA but conserving the simplicity of one-dimensional wave propagation analysis deserves further exploration.

As an additional exercise we show in fig. 34 the response spectra at the midpoint of the micro-zone for three different recorded motions. The particular results shown in the figures correspond to those obtained with the full-model, the m-DRM technique and a local model. For reference we have also added the results for a perfect half-space, which gives an idea of the frequency content of the signal and for the equivalent $1D$ model (see fig. 33). It is clear that independent of the frequency content of the input motions the results from the m-DRM technique are in very good agreement with the exact response (full-model). On the other hand it is observed how the local and the $1D$ model underpredict the response when the location of the micro-zone within the regional setup is neglected.

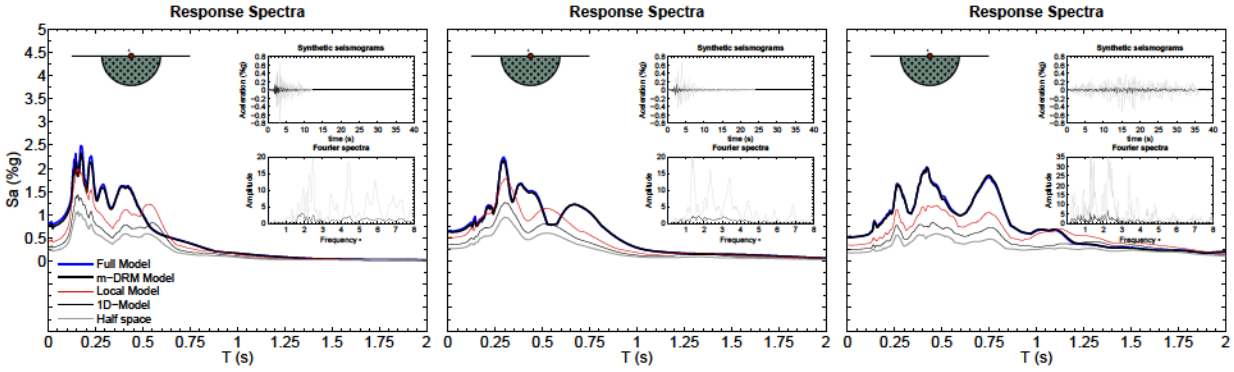

Figure 34: Response spectra for the central point of the semi-circular valley. The insert figures display the resulting synthetic seismograms and their corresponding fourier spectra together with their associated input motion.

CONCLUSIONS AND FURTHER WORK

Motivated by the multi-scale DRM technique, originally proposed by Bielak et al. (2003) and verified by Yoshimura et al. (2003b) in order to facilitate the determination of ground motions in sites located inside large-scale seismic scenarios, we have generated a computational framework intended to be used for site response analysis (SRA) by practising engineers. The proposed technique, which is a simplified version of the original DRM approach, starts from the idea of a generalized half-space containing large-scale topographic irregularities but neglecting the local site and its small-scale topography. During step-I of the modified-DRM (m-DRM) algorithm, this generalized half-space produces a regional field which is subsequently used during step-II in the analysis of the local site. The local site by itself is assumed supported by a simple homogeneous half-space and its response is determined using standard commer-

cial finite element analysis packages. In this work we have implemented a finite element code termed PIRO, which converts the regional field into effective seismic loads and interacts with the commercial code FEAP where the final site response analysis is conducted. Alternatively, the regional field may be the result of an analysis based upon the use of a uniform seismic hazard design spectra modified by a regional transfer function.

The idea of a regional field is introduced with the aid of an idealized seismic scenario conformed by a 60° V-shaped canyon submitted to incident plane *SH* waves. This particular configuration, when studied with geometrical methods reveals a finite zone adjacent to the canyon where large amplifications introduced by the canyon itself are observed. This same topography is used later in order to assess the range of applicability of the m-DRM algorithm. For that purpose a small-scale topographic irregularity resembling a micro-zone is placed in the vicinity of the V-shaped canyon. The exact response of the micro-zone is then obtained with a rigorous boundary element algorithm and the results are compared with those obtained with the m-DRM method and with a simple local analysis where the micro-zone is submitted to the original incident plane *SH* wave.

The results show that at least, for the case of incident *SH* wave fields, the modified domain reduction method is highly accurate even for the worse case scenario presented in this study where part of the topographic effect is captured by the regional field and the high frequency response is solved by the local analysis. Moreover, accuracy is maintained even when the micro-zone is located in the region where both topographies are expected to interact through trapped diffracted waves. It is then apparent that this interaction between the large and small-scale topography is not important as long as the modified optical field is representative of the main topographic features.

An interesting result is observed when the micro-zone exhibits an impedance contrast with the large scale region. In that case the results are similar to those predicted by one-dimensional wave propagation models but with strong amplifications due to the combination of the regional field and the mechanical effect. That result suggests that a method to conduct SRA based upon the classical one-dimensional wave propagation models but with an excitation corrected by regional effects should be explored.

Although in this study the proposed method has been tested for the simple case of *SH* waves, the approach seems very promising since it opens the possibility to consider at the practical level the incidence at the local site of topographic effects without the need for large computational resources. However in order to have a robust technique that can be used in the actual engineering practice the following problems must be studied.

- A similar parametric study intended to determine the influence in the response of a regional field derived from a systematically modified large-scale topography.

- The study must be extended to the case of in-plane waves and 3D cases.
- Additional simplifications required during realistic applications of the proposed technique should be considered. For instance, the effect of the homogenization of the half-space and the loss of accuracy introduced by time and space interpolation schemes required in order to couple the regional and local models must be studied.
- The study should be complemented by a realistic scenario using currently available large scale computational resources.
- The study should consider non-lineal soil response at the micro-zones. For that purpose it is convenient to extend the applicability of the computational tool PIRO to the open source computational framework OPENSEES.

Acknowledgements

This work was conducted with the financial support of EAFIT internal research fund.

REFERENCES

Assimaki, D., Ledezma, C., Montalva, G. A., Tassara, A., Mylonakis, G., & Boroschek, R., 2012. Site effects and damage patterns, *Earthquake Spectra*, **28**(S1), S55–S74.

Bielak, J. & Christiano, P., 1984. On the effective seismic input for non,Äêlinear soil,Äêstructure interaction systems, *Earthquake engineering & structural dynamics*, **12**(March 1982), 107–119.

Bielak, J., Loukakis, K., Hisada, Y., & Yoshimura, C., 2003. Domain Reduction Method for Three-Dimensional Earthquake Modeling in Localized Regions, Part I: Theory, *Bulletin of the Seismological Society of America*, **93**, 817–824.

Bielak, J., Graves, R., Olsen, K., Taborda, R., Ramírez-Guzmán, L., Day, S., Ely, G., Roten, D., Jordan, T., Maechling, P., Urbanic, J., Cui, Y., & Juve, G., 2010. The ShakeOut earthquake scenario: Verification of three simulation sets, *Geophysical Journal International*, **180**, 375–404.

Bouchon, M. & Barker, J. S., 1996. Seismic response of a hill: the example of tarzana, california, *Bulletin of the Seismological Society of America*, **86**(1A), 66–72.

Courant, R. & Hilbert, D., 2008. *Methods of mathematical physics*, vol. 1, Wiley. com.

Douglas, J. & Aochi, H., 2008. A survey of techniques for predicting earthquake ground motions for engineering purposes, *Surveys in geophysics*, **29**(3), 187–220.

Dupros, F., De Martin, F., Foerster, E., Komatitsch, D., & Roman, J., 2010. High-performance finite-element simulations of seismic wave propagation in three-dimensional nonlinear inelastic geological media, *Parallel Computing*, **36**(5), 308–325.

Elgamal, A., Yan, L., Yang, Z., & Conte, J. P., 2008. Three-dimensional seismic response of humboldt bay bridge-foundation-ground system, *Journal of Structural Engineering*, **134**(7), 1165–1176.

Fuis, G., Ryberg, T., Godfrey, N., Okaya, D., & Murphy, J., 2001. Crustal structure and tectonics from the los angeles basin to the mojave desert, southern california, *Geology*, **29**(1), 15–18.

Gallipoli, M. R., Chiauzzi, L., Stabile, T. A., Mucciarelli, M., Masi, A., Lizza, C., & Vignola, L., 2014. The role of site effects in the comparison between code provisions and the near field strong motion of the emilia 2012 earthquakes, *Bulletin of Earthquake Engineering*, pp. 1–20.

Gomez, J., Restrepo, D., Jaramillo, J., & Valencia, C., 2013. Analysis of the role of diffraction in topographic site effects using boundary element techniques, *Earthquake Science*, **26**(5), 341–350.

Hough, S. E., Altidor, J. R., Anglade, D., Given, D., Janvier, M. G., Maharrey, J. Z., Meremonte, M., Mildor, B. S.-L., Prepetit, C., & Yong, A., 2010. Localized damage caused by topographic amplification during the 2010 m [thinsp] 7.0 haiti earthquake, *Nature Geoscience*, **3**(11), 778–782.

Ichimura, T., Hori, M., & Kuwamoto, H., 2007. Earthquake motion simulation with multiscale finite-element analysis on hybrid grid, *Bulletin of the Seismological Society of America*, **97**(4), 1133–1143.

Jaramillo, J., Gomez, J., Saenz, M., & Vergara, J., 2013. Analytic approximation to the scattering of antiplane shear waves by free surfaces of arbitrary shape via superposition of incident, reflected and diffracted rays, *Geophysical Journal International*, **192**(3), 1132–1143.

Jeremic, B., 2004. A brief overview of neesgrid simulation platform opensees: Application to the soil–foundation–structure interaction problems, in *Proceedings of the Third United States–Japan Natural Resources Workshop on Soil-Structure Interaction, Vallombrosa Center, Menlo Park, California, USA*.

Jeremic, B., 2010. High fidelity modeling and simulation of sfs interaction: energy dissipation by design, *Soil-Foundation-Structure Interaction*, pp. 125–132.

Jeremić, B., Jie, G., Preisig, M., & Tafazzoli, N., 2009. Time domain simulation of soil–foundation–structure interaction in non-uniform soils, *Earthquake Engineering & Structural Dynamics*, **38**(5), 699–718.

Jongmans, D., Pitilakis, K., Demanet, D., Raptakis, D., Riepl, J., Horrent, C., Tsokas, G., Lontzetidis, K., & Bard, P.-Y., 1998. Euro-seistest: determination of the geological structure of the volvi basin and validation of the basin response, *Bulletin of the Seismological Society of America*, **88**(2), 473–487.

Kohler, M., Magistrale, H., & Clayton, R., 2003. Mantle heterogeneities and the scec reference three-dimensional seismic velocity model version 3, *Bulletin of the Seismological Society of America*, **93**(2), 757–774.

Laouami, N. & Slimani, A., 2013. Earthquake induced site effect in the algiers–boumerdes region: Relation between spectral ratios higher peaks and observed damage during the may 21st m w 6.8 boumerdes earthquake (algeria), *Pure and Applied Geophysics*, **170**(11), 1785–1801.

Lee, S.-J., Chan, Y.-C., Komatitsch, D., & Tromp, B.-S. H. J., 2009a. Effects of Realistic Surface Topography on Seismic Ground Motion in the Yangminshan Region of Taiwan Based Upon the Spectral-Element Method and LiDAR DTM, *Bulletin of the Seismological Society of America*, **99**(2), 681–693.

Lee, S.-J., Komatitsch, D., Huang, B.-S., & Tromp, J., 2009b. Effects of topography on seismic-wave propagation: An example from northern taiwan, *Bulletin of the Seismological Society of America*, **99**(1), 314–325.

Ma, S., Archuleta, R. J., & Page, M. T., 2007. Effects of large-scale surface topography on ground motions, as demonstrated by a study of the san gabriel mountains, los angeles, california, *Bulletin of the Seismological Society of America*, **97**(6), 2066–2079.

Magistrale, H., Day, S., Clayton, R. W., & Graves, R., 2000. The scec southern california reference three-dimensional seismic velocity model version 2, *Bulletin of the Seismological Society of America*, **90**(6B), S65–S76.

Magistrale, H., Olsen, K., & Pechmann, J., 2008. Construction and verification of a wasatch front community velocity model: Collaborative research with san diego state university and the university of utah, Tech. rep.

Manakou, M., Raptakis, D., Chávez-García, F., Apostolidis, P., & Pitilakis, K., 2010. 3d soil structure of the mygdonian basin for site response analysis, *Soil Dynamics and Earthquake Engineering*, **30**(11), 1198–1211.

Maugeri, M., Simonelli, A., Ferraro, A., Grasso, S., & Penna, A., 2011. Recorded ground motion and site effects evaluation for the april 6, 2009 l'aquila earthquake, *Bulletin of Earthquake Engineering*, **9**(1), 157–179.

Meslem, A., Yamazaki, F., Maruyama, Y., Benouar, D., Kibboua, A., & Mehani, Y., 2012. The effects of building characteristics and site conditions on the damage distribution in boumerdes after the 2003 algeria earthquake, *Earthquake Spectra*, **28**(1), 185–216.

Pao, Y. H. & Varatharajulu, V., 1976. Huygens principle, radiation conditions, and integral formulas for the scattering of elastic waves, *The Journal of the Acoustical Society of America*, **59**(6), 1361–1371.

Paul, A., Cattaneo, M., Thouvenot, F., Spallarossa, D., Béthoux, N., & Fréchet, J., 2001. A three-dimensional crustal velocity model of the southwestern alps from local earthquake tomography, *Journal of Geophysical Research: Solid Earth (1978–2012)*, **106**(B9), 19367–19389.

Pilz, M., Parolai, S., Stupazzini, M., Paolucci, R., & Zschau, J., 2011. Modelling basin effects on earthquake ground motion in the santiago de chile basin by a spectral element code, *Geophysical Journal International*, **187**(2), 929–945.

Preisig, M. & Jeremić, B., 2005. *Nonlinear finite element analysis of dynamic soil-foundation-structure interaction*, Ph.D. thesis, University of California, Davis.

Raptakis, D., Manakou, M., Chavez-Garcia, F., Makra, K., & Pitilakis, K., 2005. 3d configuration of mygdonian basin and preliminary estimate of its site response, *Soil Dynamics and Earthquake Engineering*, **25**(11), 871–887.

Restrepo, D., Taborda, R., & Bielak, J., 2012. Three-dimensional nonlinear earthquake ground motion simulation in the salt lake basin using the wasatch front community velocity model, Tech. rep., Final technical report, USGS Award G10AP00077.

Roësset, J. M., 1970. Fundamentals of Soil Amplification, *Seismic Design for Nuclear Power Plants*, pp. 183–244.

Schnabel, P., Seed, H. B., & Lysmer, J., 1972. Modification of seismograph records for effects of local soil conditions, *Bulletin of the Seismological Society of America*, **62**(6), 1649–1664.

Trifunac, M. D. & Hudson, D. E., 1971. Analysis of the pacoima dam accelerogram—san fernando, california, earthquake of 1971, *Bulletin of the Seismological Society of America*, **61**(5), 1393–1411.

Villalobos, F., Ovando, E., Mendoza, M., & Oróstegui, P., 2011. Damages observed in the 2010 concepción earthquake related to soil phenomena, in *Proceedings of the 5th international conference on earthquake geotechnical engineering. Santiago, Chile*.

Wang, M., Hubbard, J., Shaw, J. H., Plesch, A., & Jia, D., 2012. A Community Velocity Model (CVM) for the Sichuan basin and Longmen Shan, China, *AGU Fall Meeting Abstracts*, p. F5.

Yoshimura, C., Bielak, J., Hisada, Y., & Ferna, A., 2003a. Domain Reduction Method for Three-Dimensional Earthquake Modeling in Localized Regions , Part II : Verification and Applications, *Bulletin of the Seismological Society of America*, **93**(2), 825–840.

Yoshimura, C., Bielak, J., Hisada, Y., & Fernández, A., 2003b. Domain reduction method for three-dimensional earthquake modeling in localized regions, part ii: Verification and applications, *Bulletin of the Seismological Society of America*, **93**(2), 825–841.